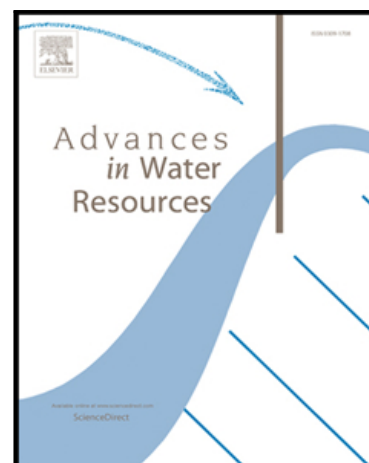


Journal Pre-proof

Bar pattern and sediment sorting in a channel contraction/expansion area: application to the Loire River at Bréhémont (France)

Florian Cordier, Pablo Tassi, Nicolas Claude, Alessandra Crosato, Stéphane Rodrigues, Damien Pham Van Bang

PII: S0309-1708(19)30521-4
DOI: <https://doi.org/10.1016/j.advwatres.2020.103580>
Reference: ADWR 103580



To appear in: *Advances in Water Resources*

Received date: 13 June 2019
Revised date: 24 March 2020
Accepted date: 25 March 2020

Please cite this article as: Florian Cordier, Pablo Tassi, Nicolas Claude, Alessandra Crosato, Stéphane Rodrigues, Damien Pham Van Bang, Bar pattern and sediment sorting in a channel contraction/expansion area: application to the Loire River at Bréhémont (France), *Advances in Water Resources* (2020), doi: <https://doi.org/10.1016/j.advwatres.2020.103580>

This is a PDF file of an article that has undergone enhancements after acceptance, such as the addition of a cover page and metadata, and formatting for readability, but it is not yet the definitive version of record. This version will undergo additional copyediting, typesetting and review before it is published in its final form, but we are providing this version to give early visibility of the article. Please note that, during the production process, errors may be discovered which could affect the content, and all legal disclaimers that apply to the journal pertain.

© 2020 Elsevier Ltd. All rights reserved.

Highlights

- Low and high bar modes originate from water discharge variations
- In turn, this induces complex compound bar formation
- Sediment sorting patterns differ between unit and compound bar patterns
- Sediment sorting does not modify bar morphodynamics if sediment mobility is high
- Floods decrease the degree of sediment sorting

Bar pattern and sediment sorting in a channel contraction/expansion area: application to the Loire River at Bréhémont (France)

Florian Cordier^{a,b}, Pablo Tassi^{a,b}, Nicolas Claude^a, Alessandra Crosato^c,
Stéphane Rodrigues^d, Damien Pham Van Bang^e

^a*Laboratoire d'Hydraulique Saint-Venant (Chatou, France)*

^b*EDF R&D LNHE - Laboratoire National d'Hydraulique et Environnement (Chatou, France)*

^c*IHE Delft (Delft, The Netherlands)*

^d*Ecole Polytechnique Universitaire de Tours & UMR CNRS 7324 CITERES (France)*

^e*INRS-ETE, LHE & Lab. CT-Scan (Québec, Canada)*

Abstract

Bars are large sediment deposits alternating with deeper areas that arise from alluvial river bed instability and forcing. The present study aimed at investigating the combined influence of flow and longitudinal width variations on the co-evolution between bar pattern and sediment sorting in a sandy-gravel river reach. To this goal, a fully non-linear 2D numerical model was developed to reproduce the morphodynamic behavior of bars in a reach of the Loire River consisting in a typical channel expansion/contraction. Numerical results showed that varying water discharge promoted a competition between low and high bar modes: i.e., from alternate to multiple bar patterns. Low bar modes were associated with coarse sediment over bar tops and fine sediment in pools, and this sorting pattern was inverted for higher bar modes. Surface sediment was coarser and the degree of sediment sorting was greater after periods of low than high flow. Due to high sediment mobility, sediment sorting did not significantly modify bar morphodynamics.

Keywords:

Fluvial morphodynamics, sediment transport, alluvial bar, heterogeneous sediment, numerical modeling, fluvial engineering.

1. Introduction

Rivers often present a wavy bed topography due to the presence of periodic bars [1], comprising large sediment deposits alternating with deeper areas (pools). In straight and weakly-curved channels, periodic bar development can enhance bank erosion, later resulting in longitudinal channel width variation, forming successions of channel expansion/contraction areas. These are typical characteristic of natural river planforms [2], where bars of different types co-exist e.g., Río Paraná (Argentina) [3], South Saskatchewan River (Canada) [4] or Middle Loire River (France) [5]. However, the mechanisms controlling bar morphodynamics in these types of geometrical forcing associated with unsteady flow remain poorly understood. Better knowledge of bar processes in expansion/contraction areas is important for river engineers and river managers, because bars actively influence riverbed topography and bank erosion, with potentially harmful consequences for navigation, water intake and infrastructure [6]. Bars also influence the hydraulics and sedimentary conditions of river channels, and consequently habitat diversity and the recruitment and succession of plant communities [7].

Duró et al. [8] distinguished two types of bar: forced, and periodic. Forced bars arise from permanent flow deformation induced by external forcing, such as change in channel geometry or steady disturbance; periodic bars arise from morphodynamic instability of the riverbed. Periodic bars include free bars, originating purely from morphodynamic instability, and hybrid bars, which like free bars, form on morphodynamically unstable riverbeds but require the presence of permanent forcing fixing their location [9, 5, 8, 10]. Over the years, stability analyses have been proposed to study the initiation conditions for free alternate bars in straight channels under constant flow [e.g. 11, 12, 13] and variable flow [14]. Analytical models were also used to study conditions leading to the formation of hybrid bars [15]. These studies showed that periodic bars were primarily governed by the width-to-depth ratio of the flow, which is a crucial parameter in determining the threshold between stable and unstable regimes, and by the bar “mode” a parameter related to the number of bars that form in the river cross-section [12], mode = 1 indicating alternate bars, mode = 2 indicating central bars, and higher values indicating multiple bars.

Bars are thus influenced by water discharge and longitudinal channel width variations, but also by the grain size distribution (GSD) and sediment mobility [16, 17, 18, 10]. For instance, braiding is enhanced by condi-

tions that are close to the initiation of sediment motion, which are typical of gravel beds [19]. Sediment size heterogeneity is an inherent characteristic of sandy-gravel and gravel-bed rivers. Sediment sorting on free alternate bars is characterized by fine sediment in pools and coarse sediment over the bar tops [16, 20, 17, 10]. In contrast, in case of multiple channels, as in braiding rivers, the sorting pattern presents coarse particles in pools and fine sediment over bar tops, with partial sediment mobility [18, 21]. Singh et al. [18] showed that no consistent sediment sorting pattern is present in case of full sediment mobility, apart from coarser sediment in the main channel, where it may strengthen resistance to erosion and play a key role in braiding [21]. However, the co-evolution between sediment sorting and bars induced by water discharge variations has yet to be investigated. Non-uniform sediment supply can modify bar morphodynamics in a complex fashion. In a straight channel initially dominated by the steady gravel bars, Bankert and Nelson [22] observed an episode of bed aggradation due to increased gravel supply, followed by an episode of bed degradation by a return to the initial sediment supply, although this did not re-establish the initial bar pattern and characteristics. Reversibility cannot be achieved, due to vertical sediment sorting processes, which highlights the relative importance of non-uniform sediment and subsequent vertical sediment sorting for bar dynamics [10].

Because width-to-depth ratio is a function of water depth and width and thus of discharge, it is a crucial parameter for bar stability and bar mode. Considering two distinct sinusoidal water flow periods, Miwa et al. [23] observed experimentally that the wave period of the flow influences the evolution of alternate bars, short-waves having more impact than long-waves. This is also illustrated by the hysteresis of water discharge/bar wavelength and water discharge/bar height, which are pronounced in case of short-waves and become smaller in case of long-waves, where the response-lag of alternate bars to change in discharge is shorter. Nelson and Morgan [24] showed that unsteady flow produces changes in bar amplitude and bar celerity compared to constant flow. Increasing or decreasing flow discharge modified *thalweg* course [25]. At falling-flow stages, sediment mainly deposited in the main channel and bar tops are eroded, while in the rising-flow stage the opposite happens, with scouring of the main channel and deposition on bars [25, 7].

Changes in channel geometry modify the local width-to-depth ratio and induce areas of erosion or deposition [1], which can trigger the development of forced bars. Bar formation driven by forced flow curvature has been predicted theoretically [e.g. 26, 27] and documented by laboratory observations [e.g.

2, 15], field investigations [e.g. 6, 28] and numerical modeling [e.g. 9, 29, 8]. Sufficient channel widening induces bar formation, while sufficient channel narrowing induces bar suppression [30, 31, 2, 19, 8]. Experimental [32, 33] and numerical [34] investigations showed that bar formation slows down the longitudinal decrease in channel width. In a sandy-gravel bed river, Rodrigues et al. [5] observed that changes in riverbank direction induced formation of chute channels, which in turn promoted local sediment deposition and led to the formation of hybrid bars.

The relationship between longitudinal channel width variations and the diversity of bar patterns was studied by Bittner et al. [35], Repetto et al. [31], Duró et al. [8] among others. Theoretical and experimental studies showed that channel expansion/contraction can promote settlement of transverse or lateral bars, and symmetrical forced bars [35, 31, 2]. Wu et al. [34] showed numerically that free alternate bars can coexist with forced transverse or lateral bars. Deeper analysis of flow structure over transverse and alternate bar configurations was carried out in a channel contraction/expansion of the Middle Loire River: Claude et al. [6] showed that the bar configuration promoted non-uniform flow distribution along the channel section, induced by bank curvature, and encouraged the transition from alternate to transverse bars and vice versa.

Duró et al. [8] showed numerically that free bars of different modes can coexist in the straight downstream segment of a channel, due to upstream width variations, which is in agreement with the Struiksmá et al. [15]’s linear theory of hybrid bars which allows incipient bars to vary longitudinally in amplitude. Duró et al. [8] also showed that imposing perfectly symmetric water and sediment flow could prevent alternate bar formation over a certain distance. Except for the study by Claude et al. [6], investigations of the morphodynamic behavior of free and forced bars in channel expansion/contraction areas all considered only constant water flow.

The objective of the present study was therefore to investigate the combined influence of flow and longitudinal width variations on the co-evolution between bar pattern and sediment sorting in a sandy-gravel river reach. A 2D fully non-linear numerical model was developed to reproduce the morphodynamic behavior of a 1 km reach of the Loire River at Bréhémont in France, where free and forced bars coexist in a channel expansion/contraction, typical of many rivers. A comprehensive set of high-quality high-resolution data including *in situ* measurements of flow, bed topography and bedload [36] has been used to build a morphodynamic model based on using the Telemac-

141 Mascaret Modeling System (TMS) (www.opentelemac.org) [10].

142 2. Materials and methods

143 2.1. Study area

144 The 1,012-km long Loire River is the longest water course in France,
145 draining a catchment area of 117,500 km² [37]. The study site (Figure 1) is
146 located in the middle reach of the river, 790 km downstream of the source,
147 in the vicinity of the village of Bréhémont (47°17'43.31"N, 0°20'33.80"E).
148 Like many rivers in Europe, the middle Loire has since the 19th century been
149 subject to training works (*e.g.* embankments, groyne construction, sediment
150 extraction) which caused canalization and incision of the riverbed, and re-
151 sulted in a modification of river morphology and in growth of vegetation in
152 the most elevated parts of the riverbed. In its middle course, the Loire River
153 presents successions of single and multiple flow patterns, featuring alternate,
154 transverse, central and multiple bar patterns [38]. The river also presents
155 secondary channels and islands which are partially submerged during flood
156 events [39].

157 The study reach presents channel widening followed by a contraction area.
158 Due to the presence of *i*) permanent embankments on the right bank imposing
159 main channel curvature; *ii*) submerged stretches of rip-rap corresponding to
160 vestiges of ancient bank protection ; *iii*) longitudinal channel width variations
161 (from 175 to 300 m) and *iv*) connection with a secondary channel permanent
162 geometrical forcings of different amplitudes are generated (Figure 1). In the
163 study reach, the average longitudinal reach slope is 0.3 m per km [41]. The
164 bed material is mainly composed of a mixture of siliceous sand and gravel and
165 is highly mobile, with a Shields number of approximately 0.10 for flowrate 386
166 m³/s, mean inter-annual flow rate being approximately 430 m³/s. Sediment
167 diameters d_{50} and d_{90} (corresponding to the 50th and 90th percentile of the
168 grain size distribution [m]) are 1.33 and 5.18 mm, respectively. The computed
169 width-to-depth ratio β in the widening part of the reach (section P80, Figure
170 1) ranges between 56 (June 19th 2010 with a water discharge of $Q_w = 386$
171 m³/s) and 159 (December 11th 2011 with $Q_w = 1950$ m³/s).

172 Nineteen field surveys corresponding to daily monitoring of an annual
173 flood in June 2010 (1,030 m³/s peak discharge) and two 2-year return period
174 floods in December 2010 (1,950 m³/s and 1,760 m³/s peak discharge) were
175 used for this study [36], together with field surveys conducted in March,
176 April, May and November 2010. Daily riverbed topography records with

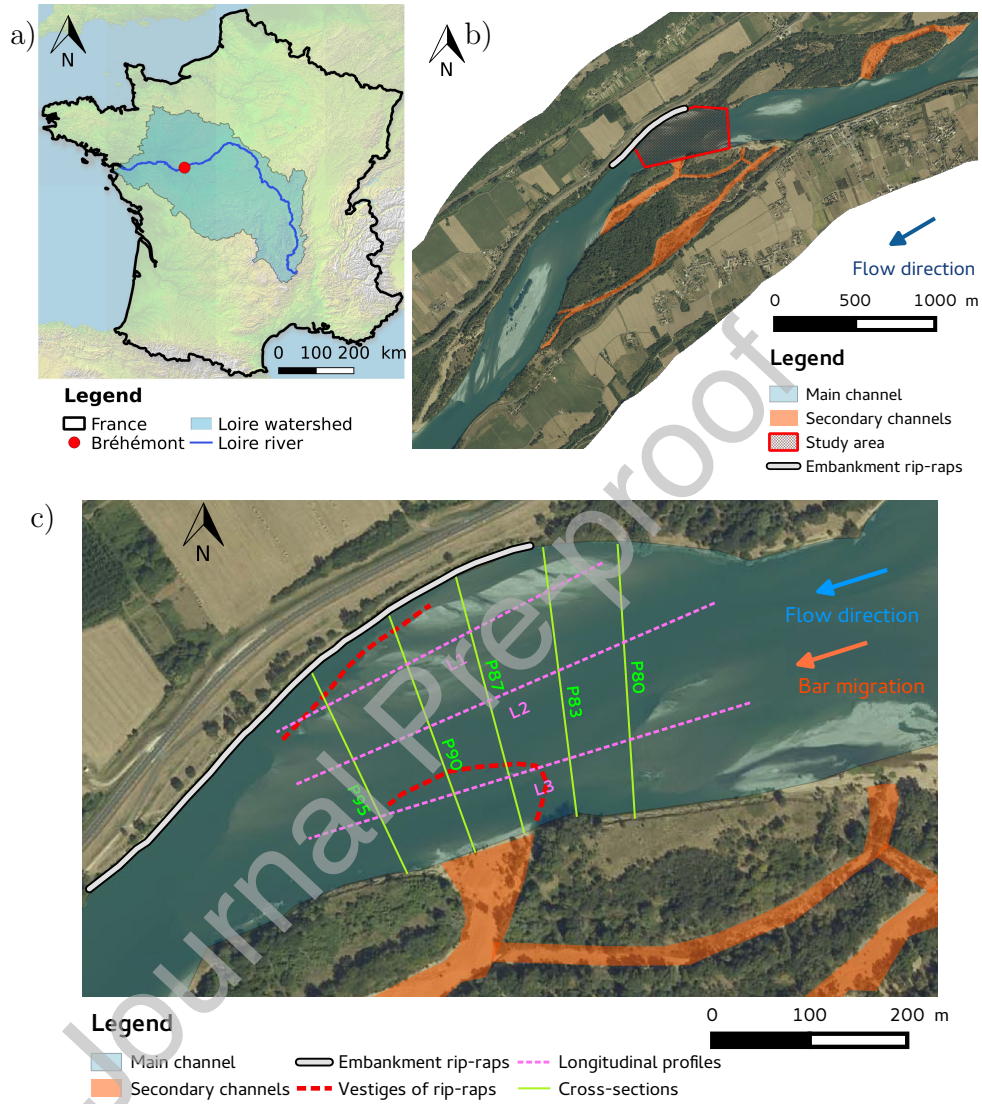


Figure 1: a) Map of France showing the location of the study reach in the Loire River watershed (credits for color-map: Shuttle Radar Topography Mission - NASA; river network = Global River Database [40]), b) medium scale aerial view of the study site taken in September 2005, showing the presence of migrating bars in the main channel and secondary channels, and c) small scale aerial view of the area of interest with the position of Claude et al. [41, 6]'s main field measurements, and the presence of geometrical forcings.

0.5 m resolution obtained by multi-beam echo-sounding were also available, together with the corresponding longitudinal water level profiles. The spatial distribution of flow velocities, measured by ADCP (Acoustic Doppler Current Profiler) during the same events, was available at three cross-sections (P80, P90 and P95; Figure 1). Claude et al. [6] estimated bedload transport rates by an isokinetic sediment sampler (BTMA), from dune celerity and geometry (i.e., dune tracking) and using the Meyer-Peter and Müller [42] and Van Rijn [43] bedload transport capacity formulae. Upstream and downstream of the area of interest, the riverbed and secondary channel topography was obtained by linear interpolation of several cross-sections measured in 2009, regularly spaced each 60 m for a distance of 2 km. Lidar data with a 0.25 m resolution collected in 2003 were used to reconstruct the floodplain and riverbanks. Supplementary information on data monitoring techniques is provided by Claude [36], Claude et al. [41, 6].

In the study area, bar migration celerity varies greatly, up to one meter per day. Complex morphodynamic processes were observed in the expansion/contraction area, with a succession of transverse bar and alternate bar configurations, in 2010 by Claude et al. [6] who concluded that the bar configuration tended to evolve cyclically with a little dependence on hydrological conditions: *i*) free alternate migrating bars cross the upstream channel expansion, *ii*) then progressively slow down and stop migrating once they progress into the expansion area, *iii*) where they shift laterally, leading to formation of a transverse bar until this reaches the opposite bank, and *iv*) the arrival of new free alternate bars from upstream resets the flow velocity field, inducing lateral erosion of the transverse bar, which then disappears from the expansion area. More details can be found in Claude et al. [6] and in Section 3. Dunes of 0.1-0.3 m height and 4-6.5 m length are present in the riverbed. According to Claude et al. [6], the flow deformation induced by this channel curvature is not enough to form forced bars, unlike what is commonly found in meanders and bifurcations.

2.2. Mathematical and numerical model

The present 2D morphodynamic model comprised two components: hydrodynamic module and morphodynamic modules [10]. The hydrodynamic module was based on the solution of the 2-D depth-averaged shallow-water equations (SWE) [44, 45, 46, 47], with a closure relationship for turbulence based on a constant turbulent eddy viscosity ν_t [m²/s], where roughness ef-

fects are parameterized through the friction law \vec{S}_f [-] of Chézy, as follows:

$$\vec{S}_f = (S_{f,X}, S_{f,Y}) = \frac{\vec{u}|\vec{u}|}{C^2 h}, \quad (1)$$

where $S_{f,X}$ and $S_{f,Y}$ correspond to the components of the friction law \vec{S}_f [-] along the longitudinal X -axis and transversal Y -axis respectively, h [m] is the water depth, $\vec{u} = (u, v)$ [m/s] is the depth-averaged flow velocity vector with components u and v [m/s] along the longitudinal X -axis and transversal Y -axis respectively, with $|\vec{u}|$ [m/s] the module of \vec{u} , and C [m^{1/2}/s] corresponds to the Chézy friction coefficient. Nikuradse [48]'s formula was used to calculate the Chézy equivalent friction coefficient, denoted $C_f = g/C^2$ [-] as a function of the equivalent roughness height of the bed associated to total friction denoted with k_s [m]:

$$C_f = 2 \left[\log \left(\frac{30h}{ek_s} \right) / \kappa \right]^{-2}, \quad (2)$$

where κ is the von Kármán coefficient ($= 0.40$ for clear water) and e is the base of the natural logarithm.

The morphodynamic module was based on the solution of the Exner [49] mass balance equation. In case of non-uniform sediment, the Exner equation was applied to every size fraction of sediment in which the mixture is subdivided. The following procedure was adopted: *i*) the sediment mixture was discretized into sediment fractions and, for each fraction, the representative sediment diameter was given; *ii*) the bedload transport capacity equation and the mass conservation formula were applied for each separate fraction of sediment.

The solution for sediment mass conservation was based on the mathematical concept proposed by Hirano [50], who developed a continuity model for vertical sediment sorting. The method is based on the decomposition of the bed into a homogeneous top layer, called *active layer*, and a *substrate* [51, 52]. Further details on the specificity of this bookkeeping active layer model can be found in Cordier et al. [10].

For each i^{th} size fraction of sediment, the sediment transport magnitude without gravitational effects $q_{b0,i} = |q_{b0,i}|$ [m²/s] was estimated using Wilcock and Crowe [53]'s bedload capacity formula as modified by Recking et al. [54]. Bedload magnitude correction to take account of gravitational effects (i.e., bed slope effects) was modeled with Koch and Flokstra [55]'s formula, where

the fractional transport rate $q_{b0,i}$ is modified as a function of the bed slope with respect to the current direction:

$$q_{b,i} = q_{b0,i} \left(1 - \beta_1 \partial_s z_b \right) = q_{b0,i} \left[1 - \beta_1 (\partial_X z_b \cos \delta + \partial_Y z_b \sin \delta) \right] , \quad (3)$$

where β_1 is an empirical coefficient taking account of the stream-wise bed slope effect, δ is the angle between the current and the X -axis, and s is the coordinate along the direction of the current. The bed slope effect is similar to a diffusion term in the bed evolution equation [56] and may smooth the bed topography and prevent numerical instabilities [57, 58]. The correction of bedload direction is given by Bendegom [59]'s relation:

$$\tan \alpha_i = \frac{q_{b,i,n}}{q_{b,i,s}} = \frac{\sin \delta - T_i \partial_Y z_b}{\cos \delta - T_i \partial_X z_b} , \quad (4)$$

where α_i is the angle between the sediment transport vector of the i^{th} size fraction of sediment and the X -axis which will deviate from the bed shear stress vector due to gravity effects; $q_{b,i,n}$ and $q_{b,i,s}$ correspond to the bedload magnitudes perpendiculars to the direction of the current and the stream-wise direction, respectively; and the coefficient T_i is calculated as $T_i = \frac{1}{\beta_2 \sqrt{\tau_{b,i}^*}}$ [60], where $\tau_{b,i}^*$ is the bed shear stress adimensionalized by the i^{th} size fraction of sediment, also known as Shields parameter, and scales the gravity effects as a function of the grain diameter of the i^{th} size fraction, and β_2 is an empirical coefficient and can be used as a calibration parameter.

The total shear stress τ [Pa] is calculated from the depth-averaged flow velocity field, where $\tau = 0.5 \rho C_f (u^2 + v^2)$, $\rho = 1000 \text{ kg/m}^3$ is the water density and C_f is equal to the sum of skin friction and bed form drag. In this study, the bed shear stress was determined as a function of the total shear stress with the relation:

$$\tau_b = \mu \tau , \quad (5)$$

where $\mu = C'_f / C_f$ is the friction factor and C'_f [-] is the equivalent Chézy coefficient due only to skin friction and is assumed to be the only component acting on bedload [61]. In the present study, C'_f was calculated assuming a flat bed using Nikuradse's formula (Equation 2), where the roughness height associated with skin friction k'_s [m] is a function of the mean sediment diameter at the bed surface with:

$$k'_s = \alpha_{k,s} \times d_{s,m} , \quad (6)$$

where $\alpha_{k,s}$ is used as a calibration parameter. García [62] summarized different values of $\alpha_{k,s}$ induced by grain size roughness measured in the field and in the laboratory ranging from 1 to 6.6, but according to Huthoff [63] in the presence of dunes this coefficient increases by several orders of magnitude: i.e., between 10 and 1000-fold.

The numerical solution of the SWE was based on the finite element method P_1 , where the advective terms are computed with the method of the characteristics. The numerical solution of the sediment transport continuity equation was performed by a procedure combining an implicit finite element scheme and an edge-based explicit upwind advection scheme, which assures mass-conservation at machine accuracy, and solution monotonicity, copes with dry zones and is easily applicable to domain decomposition [64]. Further details can be found in [10].

2.3. Numerical model set-up

The boundary conditions of the hydrodynamic model corresponded to an upstream flow discharge and a downstream free surface profile ranging [97;1,950] m³/s and [31.8;35.2] m, respectively. The downstream free surface profile corresponded to the normal water depth obtained with the Chézy formula (Equation 1) for a rectangular open channel geometry, with $C = 35$ m^{1/2}/s corresponding to the averaged Chézy coefficient measured in the site by Claude [36]. A sediment-feed (equilibrium) upstream morphodynamic boundary condition was imposed at the upstream boundary, so that the bed topography along this boundary remained unchanged during the whole morphodynamic simulation. The morphodynamic downstream boundary was set as free.

The upstream and downstream model boundaries were extended 4 km upstream and 3 km downstream by means of straight reaches of regular slope equal to $i_0 = 3 \cdot 10^{-4}$ corresponding to the average measured reach slope, in order to allow upstream flow stabilization and lessen the backwater effects in the study area. The cross-sectional profiles of the channel extensions corresponded to the most upstream (or downstream) cross-section measured in 2009 (*cf.* 2.1).

The model used an unstructured computational mesh composed of triangular elements, with a typical length of 15 m in the upstream and downstream parts of the domain. Mesh density decreased progressively to 5 m in the area of interest and in the secondary channels. The computational

time step was set at $\Delta t = 0.5$ s in order to keep the Courant number below 0.25. Mesh and time convergence analyses were conducted to ensure numerical stability and to capture local sedimentary processes. For all simulations, $\rho = 1000$ kg/m³, $\Delta_s = 1.65$, $P_0 = 0.40$ and $\nu_t = 0.05$ m²/s, with ν_t subject to sensitivity analysis using the calibrated hydrodynamic model, performed with $\nu_t \in [10^{-6} - 10^0]$ m²/s using the 1 year return flood event (i.e., $Q_{w,1y} = 1030$ m³/s). The influence of secondary currents was not accounted in the numerical model because of a negligible presence of the helical flow structure in the study site according to field observations [6] and 3D hydrodynamic simulations based on the numerical solution of the non-hydrostatic Reynolds-Averaged Navier-Stokes equations [65]. Computed water depths and velocities were affected by less than 5% for the values of ν_t considered in this range. Hence, a value of $\nu_t = 0.05$ m²/s was adopted [66]. The GSD used in the numerical model corresponds to a mixture of $F_1 = 80\%$ sand with $d_1 = 0.9$ mm and $F_2 = 20\%$ gravel with $d_2 = 3.2$ mm. Dune tracking, DoD (Differentials of DEM) [36] and suspended and bedload sediment sampling analysis [41] suggested that the transport of the sandy fraction as bedload was the most relevant sediment transport mechanism for the hydrological scenarios investigated in this work. In order to model stratigraphic processes, the riverbed was discretized into 9 vertical sediment storage layers of equal thickness, except for the deepest layer which was allowed to increase as long as deposition was on-going. The submerged rip-raps presented in Section 2.1 and Figure 1 were set as non-erodible areas of the computational domain.

2.4. Numerical model scenarios

Based on the calibrated morphodynamic model presented in Section 3, five scenarios were used to investigate the dynamics of bars and sediment sorting. The first (run A) consists in reproducing numerically the bar evolution observed *in situ* by Claude et al. [6] starting from March 15th 2010 and lasting for 1 year, using the hydrogram 2010-2011, and is referred to as the "reference scenario". To analyze the interrelations between sediment sorting and bar morphodynamics, the results of this scenario were compared versus another scenario in which sediment sorting was not taken into account (run B). In the latter scenario, grain size sorting was avoided numerically by using a thick active layer of $L_a = 100$ m: on Hirano's active layer approach, the volume fraction content of the different grain size classes are assumed to be constant in the active layer (i.e., along the vertical axis z); use of a thick active layer is a numerical artefact that prevents grain size evolution (in this

layer) since, in this configuration, mass exchanges between active layer and substrate layers become negligible. More details of this method can be found in Cordier et al. [10]. The influence of discharge on bar dynamics was investigated by comparing the results between the reference scenario (run A) and three scenarios with constant water flow (runs C, D and E): low-flow period (run C, $Q_w = 200 \text{ m}^3/\text{s}$), mean annual flow (run D, $Q_w = 500 \text{ m}^3/\text{s}$) and 2-year flood peak (run E, $Q_w = 2,000 \text{ m}^3/\text{s}$).

2.5. Analysis methods

2.5.1. Bar characteristics

Ideally, free migrating bar *fronts* are located downstream of the bar top, just before the transition with the lee side. Originally defined for dunes, the *lee side* corresponds to the transition between the bar front and the pool and has a negative slope, while the *stoss side* is used for the transition between the pool and the next bar front.

In the present study, H_b [m] denotes bar amplitude, and corresponds to the elevation between the bar top and the pool [20]. The bar wavelength λ_b [m] denotes the longitudinal distance between the two nearest bar tops separated by a pool. Migrating bar celerity in the downstream direction and the cross-sectional direction, denoted $c_{b,l}$ [m/d] and $c_{b,t}$ [m/d] respectively, is the displacement of a bar front (or bar edge) during a given time lapse. Bed evolution Δz_b [m] is the difference between the channel bed elevation at a given time with respect to the initial time (i.e., $t = 0$ s).

The most likely number of bars per cross-section, denoted m_{th} , was derived theoretically from the physics-based predictor of Crosato and Mosselman [19]:

$$m_{th} = \frac{\beta}{\pi} \sqrt{(b-3)f(\bar{\tau}^*)C_f} \quad , \quad (7)$$

where β [-] corresponds to the width-to-depth ratio of the flow, b [-] is the degree of non-linearity in the dependence of sediment transport on flow velocity (here $b=4$ as suggested by Crosato and Mosselman [19] for sandy-bed rivers), $\bar{\tau}^*$ [-] corresponds to the reach-averaged Shields number, and $f(\bar{\tau}^*) = 1.7\sqrt{\bar{\tau}^*}$ according to Talmon et al. [60]. While bar mode is mathematically defined as an integer, when derived using Equation 7 it results in a real number.

376 2.5.2. Skill and accuracy assessment

377 The root-mean-square error (RMSE) was used to compute the error be-
 378 tween field measurements and numerical results, as follows:

$$RMSE = \sqrt{MSE} = \sqrt{\frac{1}{n} \sum_{k=1}^n (m_k - o_k)^2} \quad : (m_k, o_k) \in \mathbb{R}^n \times \mathbb{R}^n, \quad (8)$$

379 where the MSE corresponds to the mean-square error, m and o are both
 380 vectors containing n scalar elements, m corresponding to numerical results
 381 and o to field observations, with k corresponding to the spatial index.

382 Error estimators such as the RMSE only inform on how far numerical
 383 model predictions differ from observations, but do not on the physical rele-
 384 vance of the computed results. Estimation of morphodynamic model accu-
 385 racy was recently introduced, using model skill scores [67, 68, 69, 70]. In
 386 the present study, the Brier Skill Score (BSS) was applied to changes in bed
 387 topography:

$$BSS = 1 - \frac{MSE_{err}}{MSE_{sig}} = 1 - \frac{\frac{1}{n} \sum_{k=1}^n (m_k - o_k)^2}{\frac{1}{n} \sum_{k=1}^n (i_k - o_k)^2}, \quad (9)$$

388 where i is a vector containing n scalar elements and corresponds to the initial
 389 topography, MSE_{err} is the error, which corresponds to the difference between
 390 model and observations, and MSE_{sig} is the signal, and corresponds to the
 391 changes in measured bed level since the beginning of the computation [70].
 392 The sign of the skill score is determined by the difference between the refer-
 393 ence data and the model prediction. $BSS < 0$ indicates that the reference
 394 initial topography is a better prediction than the model forecast. According
 395 to Sutherland et al. [67] $BSS \in [0.1 - 0.3]$ indicates reasonably/fair predic-
 396 tion, $BSS \in [0.3 - 0.5]$ good prediction and $BSS > 0.5$ excellent prediction.

397 2.5.3. Estimation of the degree of spatial sediment sorting

398 The degree of spatial sediment sorting is analyzed by calculating the
 399 statistical distribution of the mean sediment diameter in the area of interest
 400 (Figure 1). The computed distribution enables extraction of the particle size
 401 d_{s,m_χ}^- corresponding to each given decile χ , for each day of the simulation.
 402 The ratio between two opposite deciles (i.e., $d_{s,m(50-\chi)}^-/d_{s,m(50+\chi)}^-$) can be

determined to show the evolution of the degree of sediment sorting in the study area.

3. Numerical model calibration and validation

3.1. Hydrodynamic model calibration

The hydrodynamic model was calibrated on the basis of 9 permanent hydrological scenarios (3 events in June 2010, 5 in December 2010 and 1 in January 2011) using values of $k_s \in [0.05; 0.50]$ m uniformly distributed in space, updating bed topography for each scenario and calibrating on longitudinal water levels (L_1 - L_2 - L_3) and cross-sectional velocity measurements (P80-P90-P95, Figure 1). These scenarios were run 30 000 s in order to reach steady state. For each scenario, the best fitting value of k_s denoted $k_{s,cal}$ corresponded to the average value of k_s minimizing the RMSE of water depths and velocities computed along the profiles L_1 , L_2 , L_3 , P80, P90 and P95. Calibrated roughness was generally lower ($k_s = 0.11 \pm 0.04$ m) in June compared to December 2010 ($k_s = 0.205 \pm 0.09$ m) and could be hypothetically due to the bar configuration (transverse or alternate) and dune characteristics in the area of interest. Therefore, the roughness height used in the calibrated hydrodynamic model was set equal to the average value of $k_{s,cal}$, i.e., $k_s = 0.178$ m. Using the last calibrated value, the average computed RMSE on depth ranged within $[0 - 0.25]$ m, highlighting a light overestimation of water depth. Additionally, an analogous result was obtained for flow velocity, where the average computed RMSE on flow velocity ranged within $[0 - 0.16]$ m/s, highlighting a light overestimation of flow velocity (Figure 2). The present hydrodynamic model satisfactorily reproduced the spatial distribution of water depth and flow velocity in the area of interest for a given range of flow conditions from low to high flow and considering two distinct bar configurations.

3.2. Morphodynamic model calibration and validation

Morphodynamic model calibration requires computing not only relevant sediment transport rates but also a satisfactory riverbed evolution. In the present study, the coefficients used for the bed slope effects were those found in the literature, so that $\beta_1 = 1.3$ and $\beta_2 = 1.7$ [55, 60]. Active layer and sub-layer thickness was set equal at 0.40 m, and the coefficient selected for calibration corresponded to $\alpha_{k,s}$. The morphodynamic model was calibrated on the same 9 scenarios (cf. 2.4) using averaged cross-sectional bedload

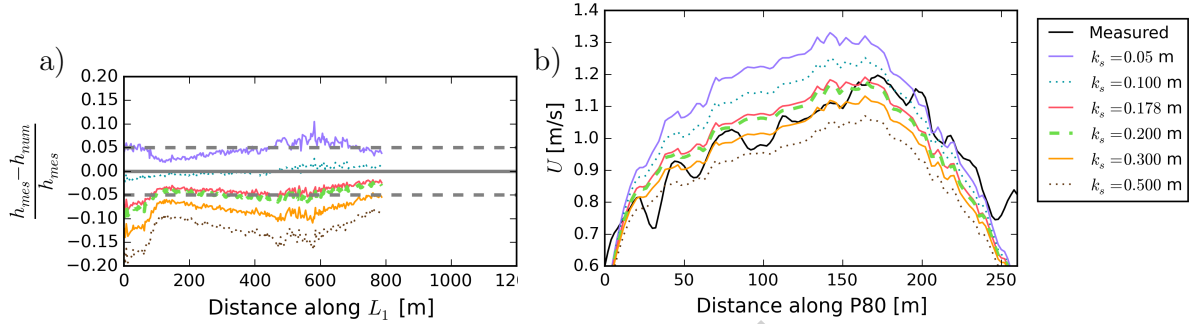


Figure 2: Example of (a) longitudinal profile of the relative error on the water free surface (gray dashed lines correspond to a relative error of $\pm 5\%$) and (b) cross-sectional flow velocity magnitude profile used to calibrate the hydrodynamic model, computed for the scenario of December 19th, 2010 with $Q_w = 701 \text{ m}^3/\text{s}$; see Figure 1 for location.

measurements (P83, Figure 1) and measured bed evolution. Calibration used short-term morphodynamic runs, in order to find the optimal value of $\alpha_{k,s}$ minimizing the difference between computed and measured transport rates for each of the 9 scenarios.

For each scenario, morphodynamic simulation started from the steady-state condition obtained with the calibrated hydrodynamic model using $k_s = 0.178 \text{ m}$, and was run for 100 s to avoid bed topography changes. Bedload fluxes were computed at cross-section P83 (see Figure 1) using values of $\alpha_{k,s} \in [1; 100]$. The best fitting value of $\alpha_{k,s}$ was then retained for each scenario. Figure 3 shows that the calibrated values of $\alpha_{k,s}$ varied as a power function of Q_w where $\alpha_{k,s} = f(Q_w) = 3.63 \times 10^6 Q_w^{-1.83}$. Because the above relation was obtained for values of $Q_w \in [386; 1,950] \text{ m}^3/\text{s}$, uncertainty on the predicted $\alpha_{k,s}$ increased greatly at low flow-rates. To compensate for eventual over-estimation at low flow-rates, a threshold value was introduced so that $\alpha_{k,s}$ remained constant for $Q_w < 300 \text{ m}^3/\text{s}$ (i.e., $\alpha_{k,s} = 106$).

The morphodynamic model was then validated by reproducing the 1 year morphodynamic event from March 15th 2010 to March 15th 2011, using the previously calibrated relation between $\alpha_{k,s}$ and Q_w . The hydrograph is presented in Figure 4. In the model, bars form further upstream of the area of contraction/expansion, through which they progressively migrate (Figure 5). Comparison between sediment transport rates measured *in situ* and computed numerically showed that the morphodynamic model computed satisfactory transport rates at distinct periods of the year and, by extension, for

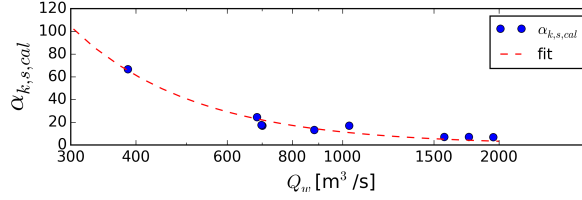


Figure 3: Power function obtained between the calibrated value of $\alpha_{k,s}$ obtained for each scenario and the associated flow-rate Q_w .

different bar configurations and flow-rates. A thorough comparison between computed and measured bed topography in terms of *RMSE*, *BSS* and patterns of erosion/deposit is presented in Section 4.1 to show that the present morphodynamic model can be used for further investigations.

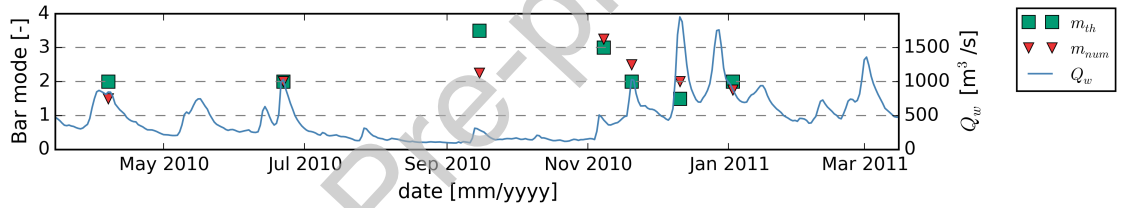


Figure 4: Time-series of the theoretical and numerical bar modes obtained with the reference scenario (scenario A) from March 15th 2010 to January 3rd 2011, and hydrograph used for the simulation.

4. Morphodynamic results

4.1. Bed evolution with variable discharge and sediment sorting

Bed evolution in the scenario with variable hydrogram with sediment sorting (which was also used for morphodynamic model validation) was obtained from a differential of bed topography between a given date and the initial time (Figure 6). The main computed bar characteristics corresponding to wavelength, amplitude, celerity and pattern are summarized in Table 1. On April 7th 2010, corresponding to the configuration of alternate bars, the upstream bar (left bank) and downstream bar (right bank) migrated downstream, following a mechanism of free bar front migration, as illustrated by the variable of bed evolution where the sediment is deposited on the lee sides and the eroded sediment from bars stoss sides. This result is consistent with

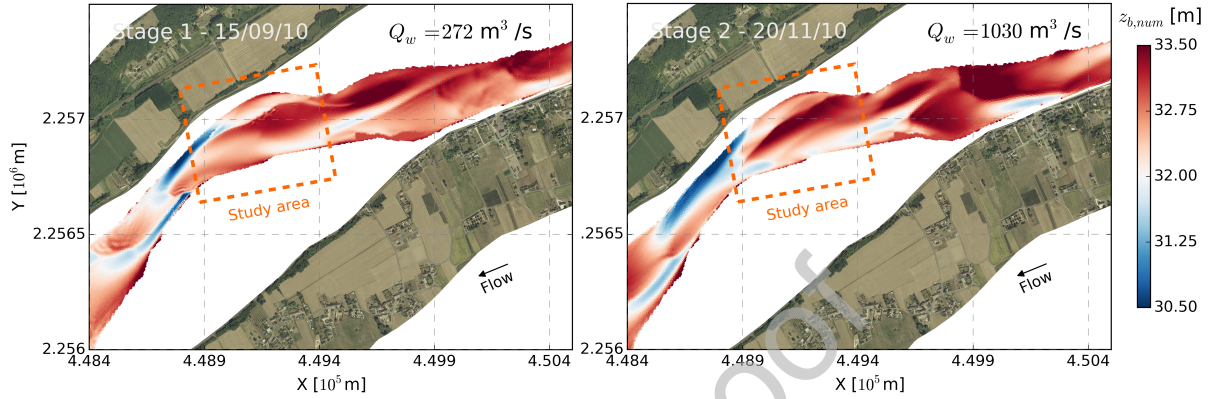


Figure 5: Macro-scale plan-view of the bed topography computed with the calibrated morphodynamic model on September 15th 2010 and November 20th 2010, showing the upstream bars having an influence on dynamics of downstream bars which are located in the area of interest. The color-scale is different from Figure 6 in order to better visualize the smaller bars forming at each side of the central/transverse bar.

those of Claude et al. [6], who measured a downstream migration celerity at 2.2 m/d, versus 2.5 m/d numerically (Table 1). According to field measurements, the alternate bar system progressively evolved toward a different bed configuration, with the presence of a transverse bar, as seen on June 22th 2010 (Figure 6A2, B2). Numerical results also showed the formation of a transverse bar front, corresponding to a left side bar which not only migrated rapidly downstream at a celerity of 6.8 m/d, but also expanded rapidly in the direction of the right bank at a celerity of 2.1 m/d, restricting the *thalweg* along the right bank to a narrow strip scaling from 1/3 to 1/4 of local channel width. The migration front and the edge of this bar were characterized by high local bed slopes (Figure 6A2, B2). In turn, this migrating structure induced not only erosion of the right side bar, by deviating the flow toward the right bank and increasing local bed shear stress as observed by Claude et al. [6], followed by formation of an upstream left side channel. Given this configuration, the numerical results show that upstream pools moved progressively from the right to the left bank, while the opposite trend was observed downstream, indicating an inversion of the *thalweg* path in the study area. The behavior observed downstream were in agreement with field observations, while this comparison cannot be easily drawn upstream mostly

because field data is not available immediately upstream of the study area.

From the end of June to November 2010, during the period of approximately 4 months of seasonal low flow, riverbed topography also underwent important changes, as illustrated by the measurements and numerical results on November 8th 2010 (Figure 6A3, B3). During this period, the transverse bar tended to move toward the right bank [6]. According to Figures 6B2 and B3, the upstream left side channel presented above, observable in the early stage of its formation on June 22nd 2010, tended to concentrate the flow along the left riverbank in a narrow strip of approximately 1/3 local channel width. This led to alternate left-side bar erosion, and the development of a central bar in the area of interest, which stabilized along the longitudinal direction, seen in a migration celerity close to 0 in the longitudinal direction on September 15th 2010 (Figure 5a and Table 1). Under this configuration, flow was concentrated in the *thalweg*, located at the left and right sides of the central bar, triggered the formation and migration of shorter and smaller bars, as illustrated in Figures 6B3 and 5. Progressively, the central bar migrated toward the right bank at a celerity of approximately 1.2 m/d, corresponding to a transition between transverse and central bar, as seen on November 20th 2010 (Figure 5b). Such a bar pattern was not observed in the field, but could have been overlooked due to a lack of field observations in this period of time [36].

The left-side alternate bar front visible on November 20th 2010 (Figure 5b) and located immediately upstream of the study area migrated progressively downstream, before becoming visible (in both the field and numerical model) in the study area on December 13th 2010 (Figures 6A4, B4). The left bar deviated the flow toward the right riverbank and inverted the *thalweg* path, which eventually followed the same pattern as seen on April 7th 2010. As a result, the transverse bar tail migrated downstream at a celerity in the range of [5.1-9.5] m/d, and was pushed toward the right bank at [2.2-2.5] m/d, while the transverse bar front in the channel contraction area remained immobile. This bar eventually became the right-side alternate bar observed on January 3rd 2011 (Figures 6A5, B5), where the bar lee side and edge were characterized by a steep slope which migrated toward the right bank.

These results suggest that the computed amount of erosion and deposition underlying the observed bar migration was in agreement with the measurements [6]. This behavior is not only depicted by the planform distribution of bed topography and bed evolution (Figure 6), but also by the relatively low values of $RMSE(\leq 20 \text{ cm})$ computed between measured and computed

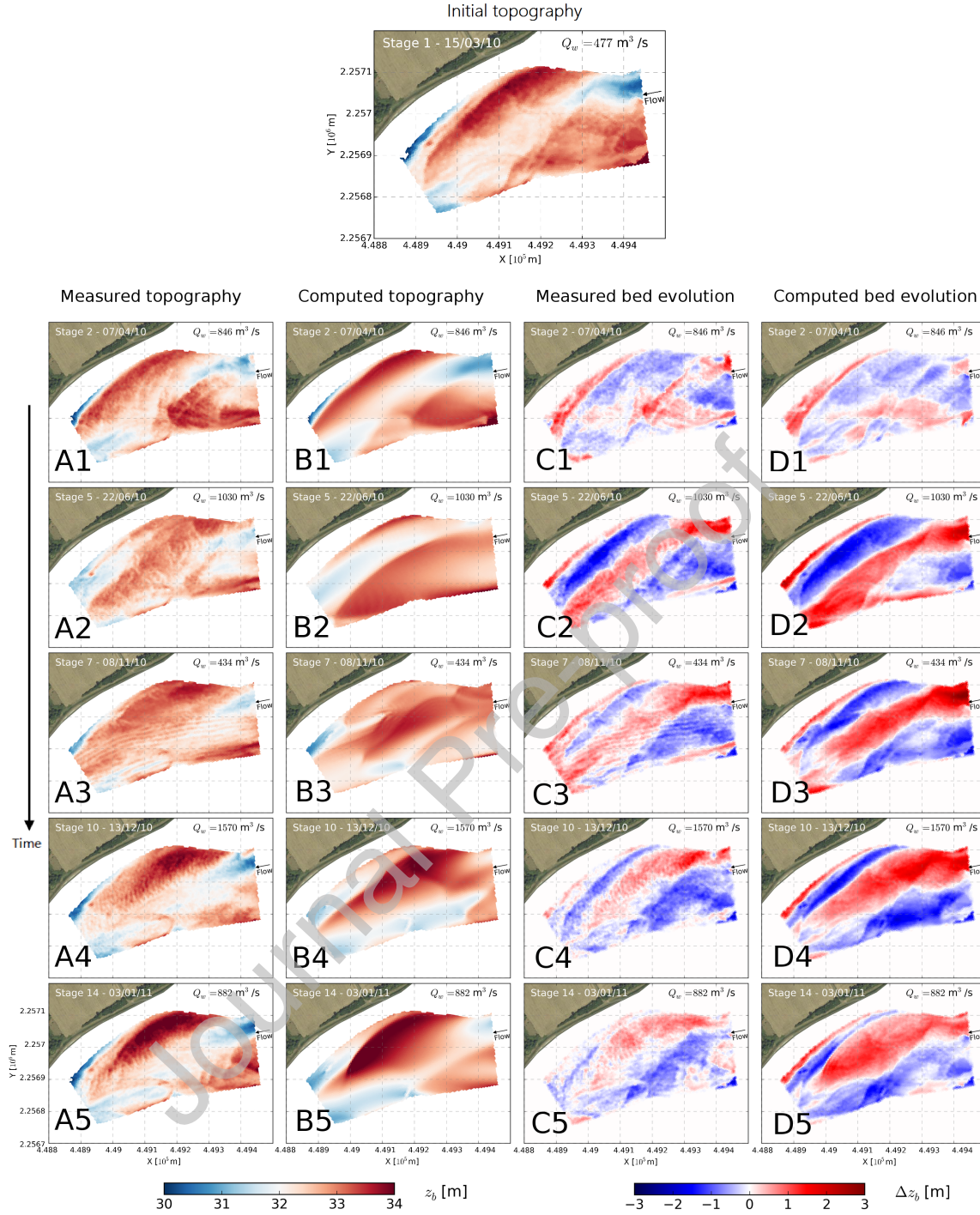


Figure 6: Plan-view of bed topography and bed evolution measured in the field and computed with the calibrated morphodynamic model from March 15th 2010 to March 15th 2011.

Table 1: Bar characteristics computed at different stages of the simulation taking account of sediment sorting (scenario A).

Date [dd/mm/yyyy]	Q_w [m ³ /s]	β [-]	λ_b [m]	H_b [m]	$c_{b,l}^*$ [m/day]	$c_{b,t}^*$ [m/day]	Bar pattern **	m_{th}^{***}	m_{num}^{***}
07/04/2010	846	95	1340	1.4	2.5	1.3	A	2	1.5
22/06/2010	1030	86	1510	1.3	6.8	2.1	T	2	2
15/09/2010	272	≈ 200	1440	1.3	≈ 0	1.2	C	3.5	2-2.5
08/11/2010	434	142	1180	1.3	≈ 0	≈ 0	C/T	3	3-3.5
20/11/2010	1030	82	1410	1.5	7.9	1.1	T	2	2.5
11/12/2010	1950	56	1410	1.9	9.5	2.5	A	1.5	2
03/01/2011	882	88	1260	2.0	5.1	2.2	A	2	1.5 - 2

time
↓

* Bar celerity was measured over a period of 10 consecutive days, subscript l (or t) is used for the velocity component in longitudinal downstream (or cross-sectional right-side) direction ;
 ** Subscripts used to denote bar configuration: A=Alternate bars; C=Central bar; T= Transverse bar ;
 *** m_{th} and m_{num} denote the bar modes computed theoretically with $b = 4$, $C_f = 0.008$, $B = 225$ m and $d_{s,m} = 1.36$ mm, and obtained numerically on the P83 cross-section (see Figure 1), respectively.

bed topographies (Figure 7). BSS was $[0.26 - 0.46]$, which seems reasonably good, considering the complexity of the morphodynamic processes taking place in the study area. BSS increased progressively from March 15th 2010 to June 25th 2010, and then decreased progressively until January 3rd 2011. This trend is explained by the fact that the reference bed topography used to compute the skill score was associated with an alternate bar configuration. Consequently, the lowest BSS s were generally reached when the model predicted an alternate bar pattern, and vice versa, the highest when the bar pattern was far from the initial configuration (i.e., transverse, according to Figure 7).

No clear relationship between flow-rate and computed bar characteristics emerged (Table 1). On the whole, the computed bar amplitudes and wavelengths were of the same order of magnitude as the values measured in the field, where computed bar wavelengths varied in a range of $[1180-1510]$ m vs. $[1000-1140]$ m in the field, and computed bar amplitudes varied in a range of $[1.3-2.0]$ m vs. $[1.29-2.20]$ m [6]. The consistency observed between the bed topography measured in the field and computed numerically with the reference scenario (Figure 6) shows that the morphodynamic model was able to reproduce the main processes of bar migration in the study area.

The largest differences were found in the magnitude of computed bed evolution, which was generally greater than in the field (Figure 6, e.g. A5,

B5). This difference could be attributed to two causes: firstly, the spatial variation of dunes over bars observed in the field [6], which could not be represented with the current modeling approach, and which was assumed also to play a role in the spatial non-uniformity of bed shear stress; and secondly, the suspended sediment transport, which was not modeled but could increase diffusion and decrease the intensity of bar topography [71] in the same way as observed for dunes [72].

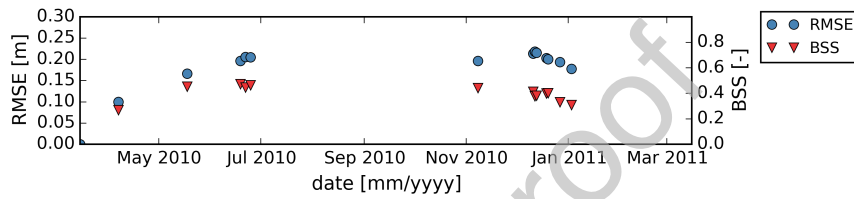


Figure 7: Time-series of RMSE and BSS computed on bed topography, taking account of sediment sorting (scenario A), from March 15th 2010 to January 3rd 2011.

4.2. Bed evolution with variable discharge without sediment sorting

A thorough comparison was then performed on bed topography and bed evolution computed with (scenario A) and without taking account (scenario B) of sediment sorting. The first approach consisted in comparing planform bed topography and bed evolution at a given stage of the simulation between the two scenarios. Two stages were used for this comparison, the first one to the end of the low flow period on November 8th 2010, and the second corresponding to the end of the 2-year flood event on January 3th 2011. Results (Figures 6B3, B5 vs. 8) showed that the difference between computed topographies for the two scenarios was relatively small with respect to the bed elevation changes occurring in each of these scenarios.

4.3. Bed evolution with constant water flow

Figure 9 illustrates the long-term response of the alluvial riverbed using three distinct constant water discharges in the expansion area, considering water discharges representative of the low-flow period (run C), mean annual flow (run D) and 2-year peak flood (run E). Results showed that in every single scenario at constant flow-rate, a dominant bar pattern was observed in the expansion area in the late stage of the simulation. In run C, bed topography consisted of in a multiple channel pattern, where relatively short bars

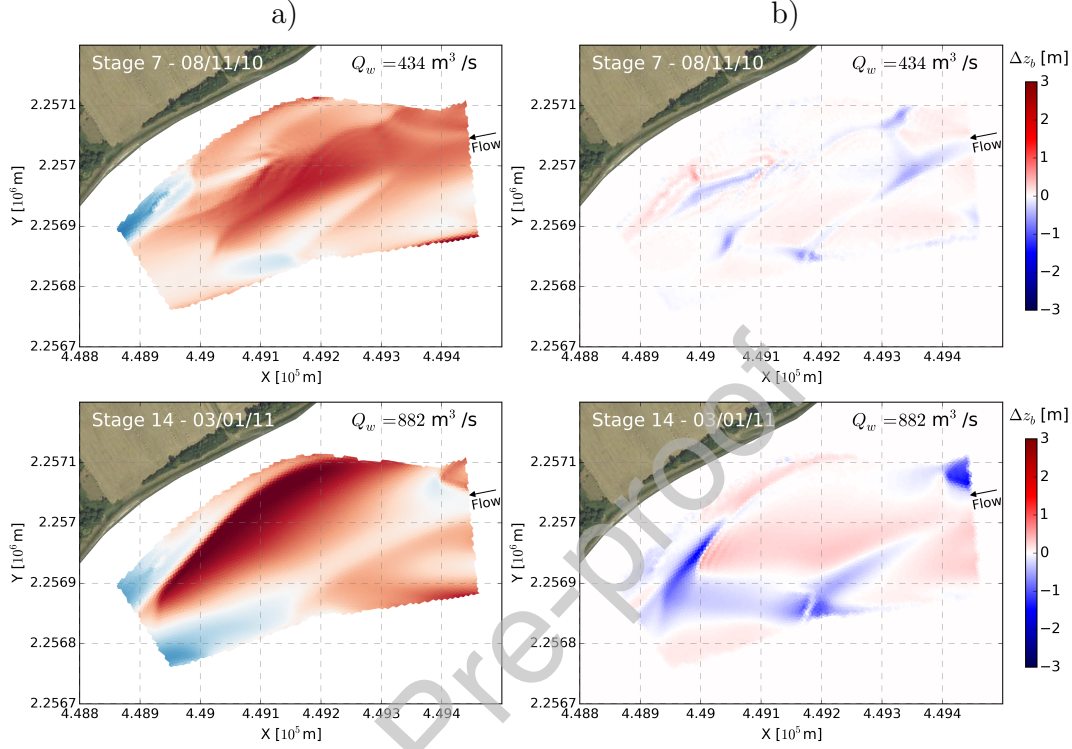


Figure 8: Plan-view of a) bed topography computed without taking account of sediment sorting (scenario B) and b) difference in computed bed topography at the same date between scenarios with (A) and without taking account of sediment sorting (B). The black squares correspond to twelve points distributed close to the left bank, the right bank and the center of the channel along the P80, P87, P90 and P95 cross-sections, which were used to compare results from runs A and B.

continually migrated downstream and reworked the main channel riverbed. Conversely, in run E, the riverbed was characterized by alternate bars, which were particularly elongated and stopped migrating. In run D, an intermediate state was obtained, where transverse bar and central bars patterns are alternated over time, with moderate bar migration celerity. Comparison between these three runs showed that higher water discharge invariably decreased the long-term computed bar mode and induced simpler channel patterns.

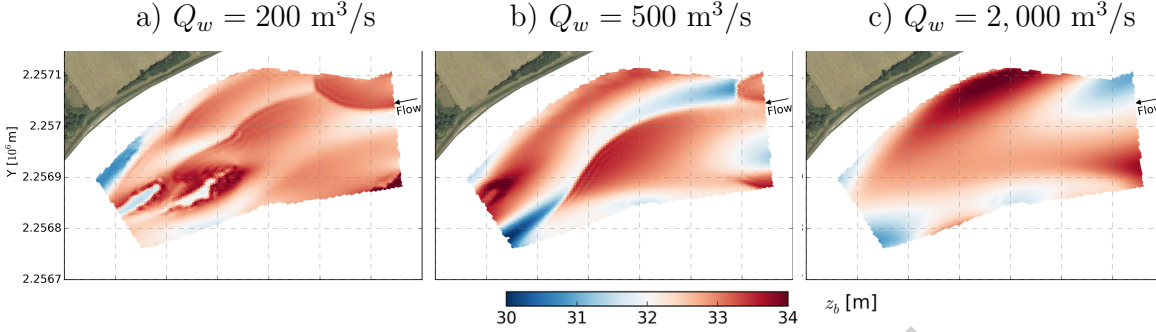


Figure 9: Plan-view of bed topography computed with the morphodynamic model after a period of 300 days with constant inflow, representative of a) the low-flow period (run C), b) mean annual flow (run D) and c) 2-year peak flood (run E).

4.4. Bar mode

Computation of the most probable bar mode using Crosato and Mosselman [19]’s predictor at different stages of the reference scenario (Table 1) and bar modes obtained from the numerical model (i.e., scenario A) suggested a strong variation in bar pattern in the study area, between alternate bars ($m = 1$), central bars ($m = 2$) and a multi-channel or braided pattern ($m \geq 2.5$).

Theoretical bar modes suggested that alternate bars could only develop in the study area at relative high flow-rates, i.e., during the 2-year flood peak of December 11th 2010 (Figure 4), with $\beta \approx 50$ (Table 1). Likewise, the theory suggested that centrals bars (i.e., $m = 2$) are dominant at flow-rates around the 1-year flood discharge of $Q_w \approx 1000 \text{ m}^3/\text{s}$, corresponding to $\beta \approx 90$. These relatively simple bar patterns (i.e., alternate, central and transverse bars) were also computed numerically during periods of high flows. Moreover, the theory predicts higher bar modes at lower flow-rates, with multi-channel bar patterns around the mean annual, flow-rate: i.e., for $\beta \approx 100$. Similarly, more complex bar patterns were obtained numerically during periods of low flow (Figure 4).

4.5. Sediment transport

The spatial distributions of computed bed shear stress and bedload magnitude were similar, as depicted in Figure 10. This outcome was expectable, as computed sediment transport rate is primarily a power function of bed

611 shear stress, which is scaled by the total shear stress, which in turn is a func-
 612 tion of depth-averaged flow velocity (see Equation 5). The strong correlation
 613 between the spatial distributions of flow velocity and bed shear stress sug-
 614 gests that computing bed shear stress from total shear stress (see Equations
 615 5 and 6) does not significantly impact the spatial redistribution of bed shear
 616 stress. Since shear stress and sediment transport are strongly correlated,
 617 interest will focus particularly on the computed sediment transport in this
 618 section.

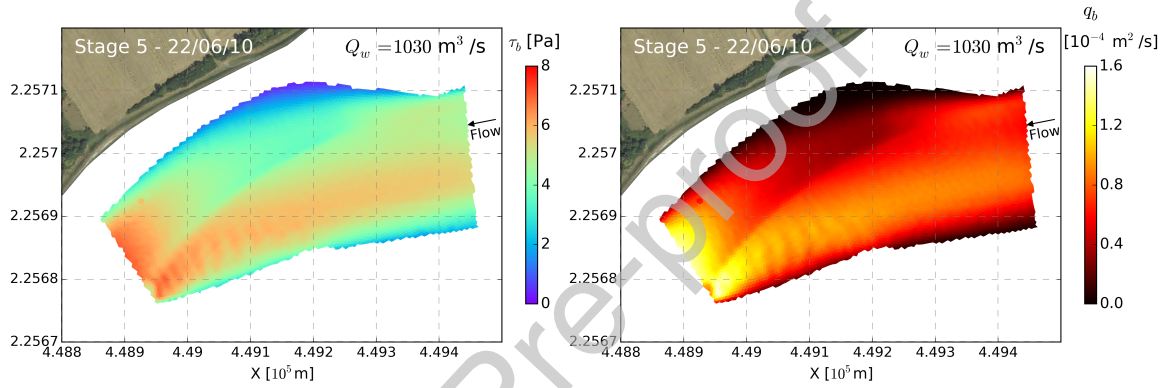


Figure 10: Plan-view of bed shear stress and bedload magnitude computed with scenario A with the transverse bar configuration on June 22th 2010, both displaying similar spatial distributions.

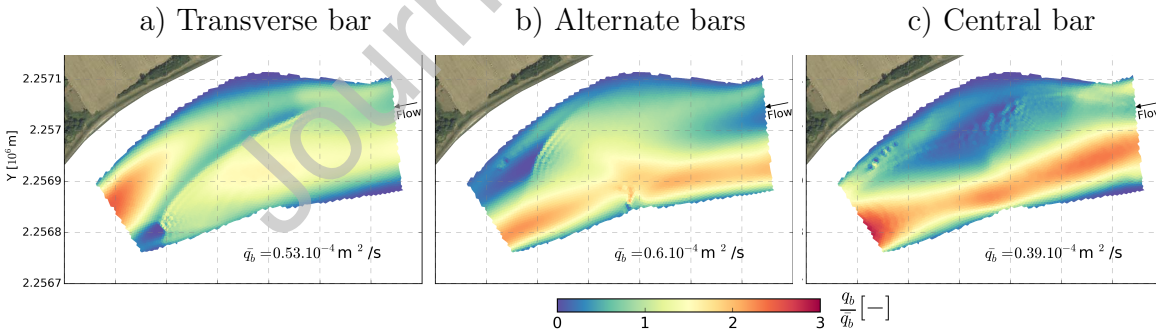


Figure 11: Plan-view of the ratio between bedload magnitude and spatially averaged bedload magnitude computed with scenario A considering the configuration of a) central bar (September 15th 2010), b) a transverse bar (June 19th 2010) and c) alternate bars (January 3rd 2011).

Figure 11 illustrates the patterns of normalized sediment transport (i.e., q_b/\bar{q}_b) obtained numerically with different bar configurations. The spatial distribution of sediment transport rates (and thus bed shear stresses) is seen to be drastically different in case of transverse bar, alternate bars, or more complex bar patterns, i.e., depends on the bar configuration. In the transverse bar configuration (Figure 11a), sediment transport was relatively high (i.e., $q_b/\bar{q}_b > 1.5$) over the bar head, while it dropped to 0 in the immediately downstream adjacent pool visible on June 19th 2010, and decreased strongly along the bed slope formed by the transverse bar edge (see Figure 6B2 for locating bar fronts). Bedload in the *thalweg* close to the right bank tended to increase progressively in the downstream direction, and was of the same order of magnitude as bedload over the transverse bar. In the alternate bar configuration (Figure 11b), high sediment transport rates (i.e., $q_b/\bar{q}_b > 1.5$) were distributed along the left riverside, i.e., over the left migrating alternate bar and in the adjacent downstream pool, where the transition between the left bar/pool sequence featured a local moderate longitudinal decrease in sediment transport. Along the right riverside, sediment transport increased longitudinally from the upstream pool until the downstream bar front, and dropped to low values ($q_b/\bar{q}_b < 0.5$) in the immediate downstream pool (see Figures 6B1, B5 for locating bar fronts). In more complex bar configurations, with a central bar (Figure 11c), sediment transport was maximal on the left side of the channel, where the flow and high bed shear stress were concentrated. Moreover, sediment transport over bar tops was much lower than in the alternate or transverse bar configurations, as the flow tended to concentrate in the narrow *thalweg*.

For all bar configurations, in the channel expansion area sediment transport was very low close to the left and right riverbanks. This may have been due to energy dissipation by water motion on the river banks and sheltered areas induced by changes in bank direction, and coincided with the low flow velocities observed in these areas by Claude et al. [6]. In addition, the spatial distribution of bedload magnitude showed that the highest gradients were located at the bar front and bar edges (Figures 5 and 6), which suggests that, elsewhere, sediment transport rates tended to vary more smoothly. In general, the computed bedload was 3-5 fold greater higher over submerged bars (i.e., except for central/transverse bars, which are not fully submerged) and in the deep channel than in the lee-side and pools, and this difference was greater for lower water discharges.

The temporal variation in the spatially averaged sediment transport rates

in the study area (Figure 12) showed similarities with the hydrogram, especially during the period of low flow, although differences could be easily detected, such as in February 2011. This analysis suggests that sediment transport, in the study area, not only varied as a function of hydrological conditions, but also depended on local variations in sediment supply, due to continuous bar migration in the study area. The temporal variation in the ratio between average sand transport rate and sand over total bedload suggests that sand contributed approximately 84% of bedload transport in the study area during the simulation, and varied only slightly within a [82-87]% interval. This result also shows that the proportion of sand transport with respect to total transport decreased rapidly in the beginning of the simulation and tended to stabilize during the run.

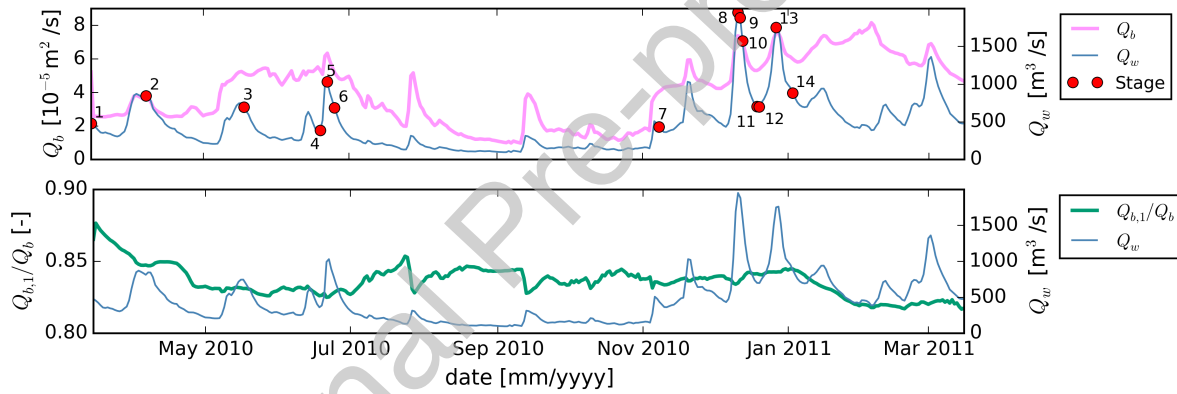


Figure 12: Time-series of spatially averaged sediment transport rate and ratio between spatially averaged transport rates of the finest class of sediment and total bedload in the study area, computed with scenario A from March 15th 2010 to March 15th 2011.

Figure 13 shows the planform distribution of the deviation angle between the bedload and flow velocity vector fields for the transverse and alternate bar configurations. Sediment transport was always redirected toward the down-slope, as formulated in the model (Equation 4). Consequently, the largest angles of deviation were found at bar fronts and bar edges, and scale up to $\pm 5^\circ$. The transverse bar and right alternate bar edges being oriented toward the right riverside (Figures 6B2, B5), sediment transport was then deviated toward the right bank (Figure 13), favoring lateral migration of bars. In the transverse bar configuration (Figure 13a), the remnant of the right side alternate bar deviated the sediment toward the *thalweg*, which

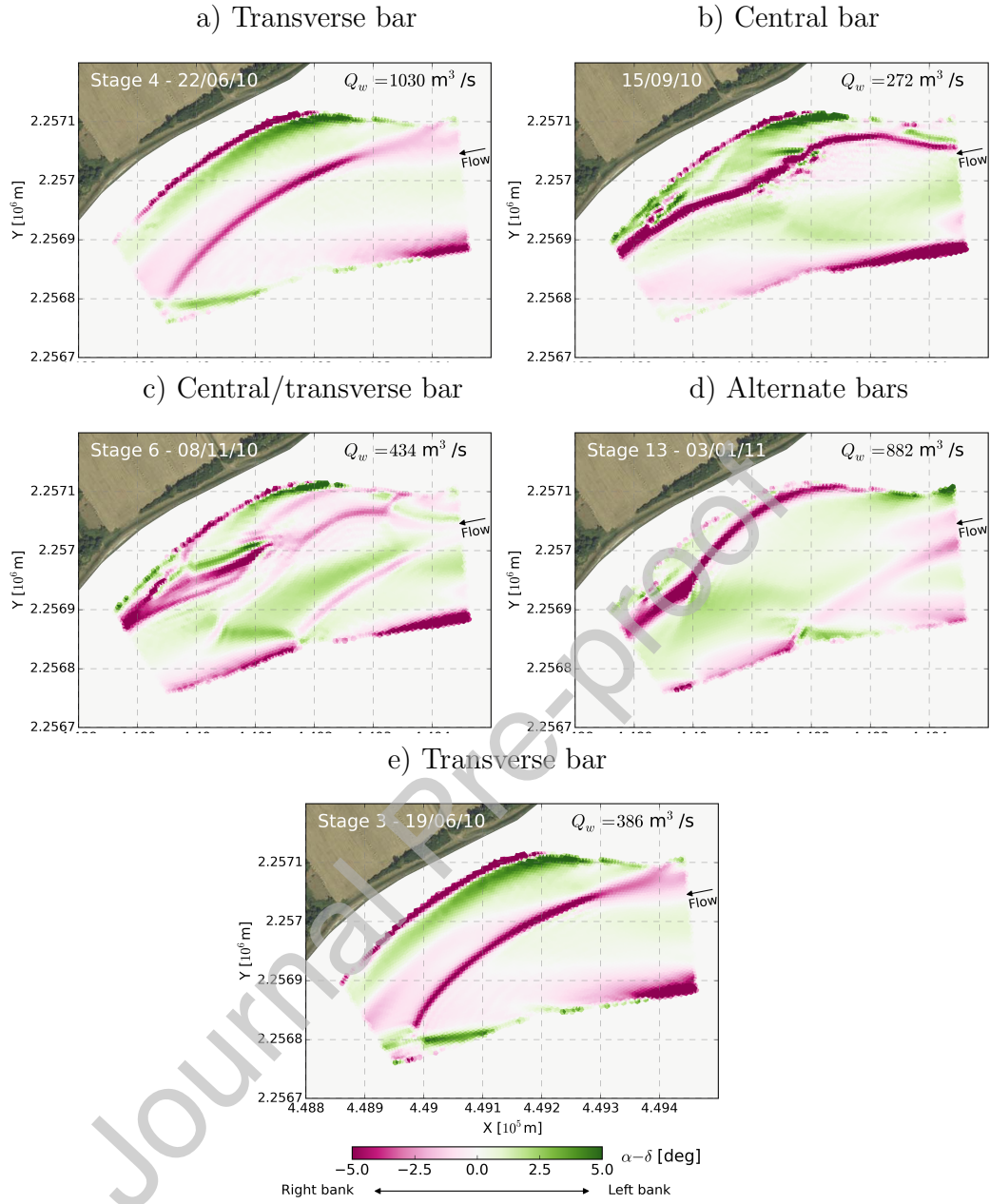


Figure 13: Plan-view of the angle of bedload deviation, computed with scenario A with a) the transverse bar on June 22th 2010, b) alternate bars on January 3rd 2011, c) central bar on September 15th 2010, d) central/transverse bar November 8th 2010, and e) transverse bar on June 19th 2010. The arrow below the color-scale indicates the direction of the deviation angle, where negative values directed toward the right riverbank and positive values toward the left riverbank.

was restricted to the right side of the transverse bar edge (Figure 6B2). Because the computed bedload was low along the right riverside, erosion of the remnant right side alternate bar was slow. While deviation angles were found to be generally low over the transverse bar ($|\alpha - \delta| < 1.5^\circ$), they were larger over the right alternate bar head ($|\alpha - \delta| > 1.5^\circ$), where the sediment located over the bar head was moderately deviated toward the left bank, i.e., in the *thalweg*. As a result, in the alternate bar configuration, the right bar migrated not only laterally, but also longitudinally.

Sediment transport directions with the transverse bar and alternate bar configurations are compared in Figure 14. In the transverse bar configuration, sediment transport along the right side of the channel was mainly directed toward the left riverside, in comparison with alternate bars, and vice versa in the center-left sides of the channel, where sediment transport was mainly directed toward the right riverbank in the transverse bar configuration, in comparison to alternate bars. The largest absolute deviation angles were found at the exact location of alternate and transverse bar fronts and edges, and sometimes exceeded 15° . This result is consistent with the previous outcomes (Figure 13), showing that bedload deviation and bar geometry are interdependent. It also shows that switching from a bar configuration to another configuration tended to re-balance the bedload directions from the center-left side to the right side of the channel.

The sediment transport vector fields of June 19th 2010 and June 22nd 2010 were compared to estimate the influence of water discharge on sediment transport direction (Figure 13a vs. 13e). These two events were selected because their computed bed topographies were similar, with weak ($Q_w = 386 \text{ m}^3/\text{s}$) and relatively high ($Q_w = 1030 \text{ m}^3/\text{s}$) water discharge, respectively. The higher color contrast in low than high flows shows that decreasing water discharges were followed by increased bedload vector field deviation in the downslope direction; this is in agreement with the higher bedload deviations computed over the central bar and central/transverse bars at low water discharges in comparison with alternate and transverse bars at relatively high flow-rates (Figure 13b,c vs. 13a,d).

4.6. Sediment sorting

The planform distribution of mean sediment diameter at the bed surface (i.e., in the active layer) provides initial information on processes of sediment sorting over bars (Figure 15). In the alternate or transverse bar configurations, coarse sediment was located over bars, but also in the main

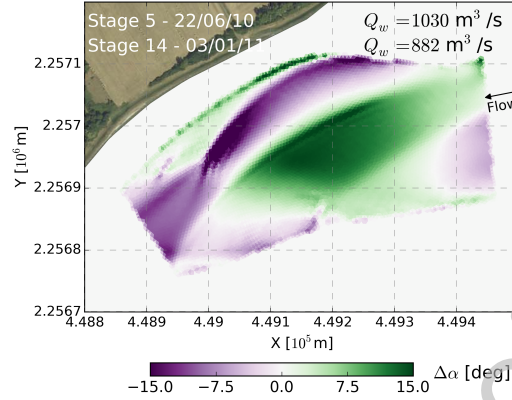


Figure 14: Plan-view of the angle between bedload transport directions computed with scenario A with the transverse bar on June 22nd 2010 and alternate bars on January 3rd 2011. Negative angle values, depicted in purple (and positive values in green) signify that the bedload vector computed with the transverse bar was more directed toward the left (right) bank, respectively, with respect to the bedload vector computed with alternate bars.

channel, while fine sediment concentrated in pools located at the immediate down-slope of bar heads and edges (Figures 5 and 6). Longitudinal and cross-sectional stratigraphic profiles of transverse and alternate bar configurations (Figure 16a,b) confirmed the later outcome and also helped to characterize vertical sediment sorting in the bar-pool sequence: computed bed stratigraphy consistently showed a surface layer that was coarser than the sub-layers over bar tops and stoss sides (e.g. Figure 16a along *L2* from 200 m to 400 m and Figure 16b along *L2* from 100 to 450 m), and in the main channel (e.g. Figure 16a along *P90* from 150 to 200 m and Figure 16b along *P90* from 30 to 50 m). In contrast, the sub-layers located below pools and bar lee sides were generally composed of coarser sediment than the surface layer (e.g. Figure 16a from 80 m to 160 m along *L2* and Figure 16b from 210 m to 240 m along *P90*). This resulted in coarse surface bars tops covering a large amount of finer sediment in the sub-surface. Sediment sorting differed in the central/transverse bar configuration (Figure 5b). While the longitudinal sediment sorting was similar to that in the previous bar configurations, the cross-sectional sorting pattern differed (Figure 16c), the coarsest sediment being located in the main channel (from 0 m to 70 m along *L2* and from 20 m to 70 m along *P90*), while $d_{s,m}$ decreased progressively transversally

(i.e., perpendicular to the bar edge) and was lowest over the bar top (from 70 to 140 m along *P90*). As a result, the central/transverse bar surface was composed of fine sediment, progressively coarsening in the deeper layers.

On the other hand, the increasing color contrast on September 15th and November 8th 2010 (see Figure 15) suggests that the degree of surface sediment sorting was higher during the period of low than medium or higher flows. This is also shown by the variation of $d_{s,m90}/d_{s,m10}$ which characterizes the sediment sorting at the bed surface.

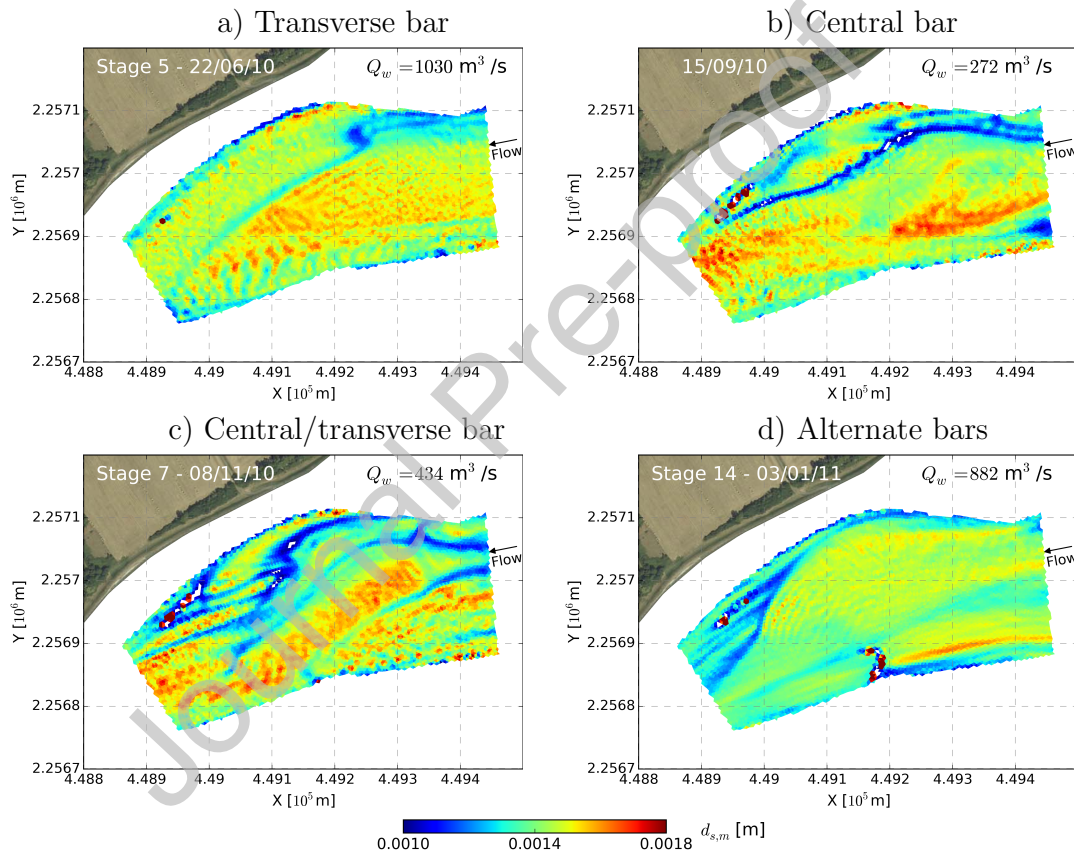


Figure 15: Plan-view of mean sediment diameter at the bed surface computed with scenario A considering configurations with a) transverse bar (June 22nd 2010), b) central bar (September, 15th 2010), c) central/transverse bar (November 8th 2010) and d) alternate bars (January 3rd, 2011).

Mean surface sediment diameter increased rapidly in the early stages

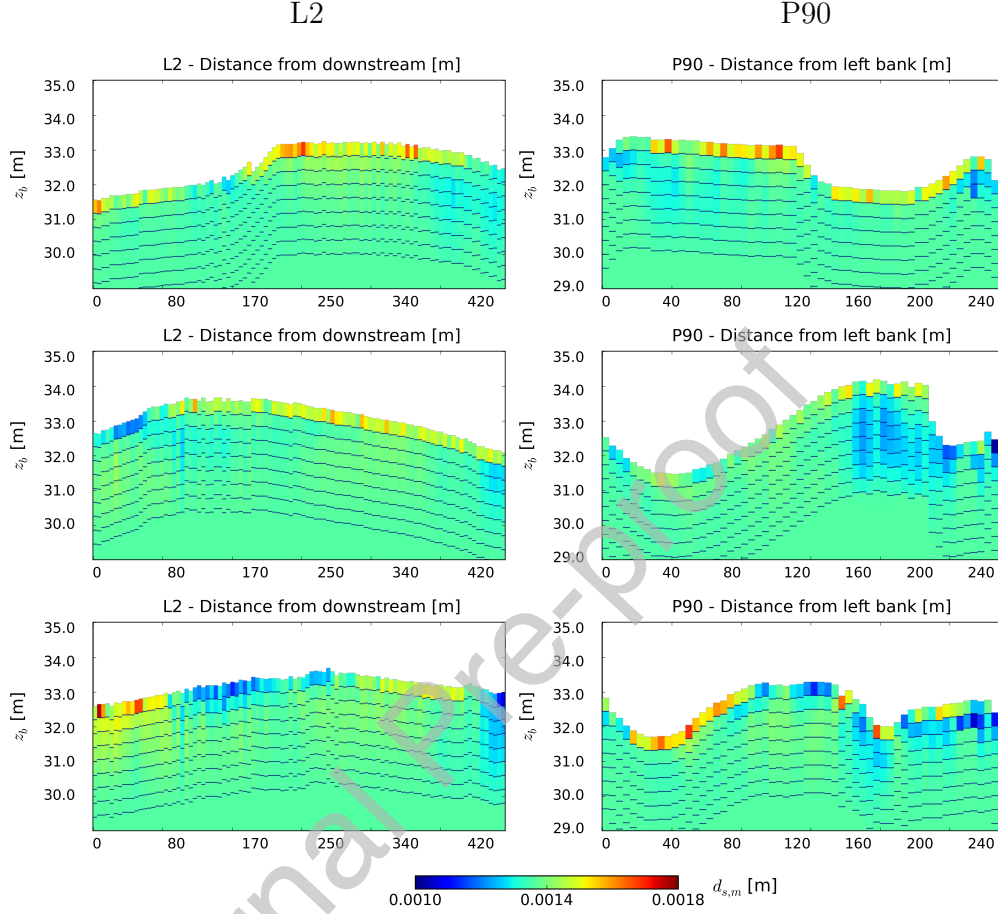


Figure 16: Longitudinal (L2) and cross-sectional (P90) stratigraphic profiles computed with scenario A with the configuration with a) transverse bar (June 22th 2010, $Q_w = 1,030$ m³/s), b) alternate bars (January 3rd 2011, $Q_w = 882$ m³/s) and c) central/transverse bar (November 8th 2010, $Q_w = 434$ m³/s). See Figure 1 for location of L2 and P90.

of the simulation, but then rapidly stabilized before oscillating toward an equilibrium value of ≈ 1.42 mm (Figure 17a). On the other hand, in the sub-layers, mean diameter decreased during the simulation (Figure 17a). Wide fast mean sediment diameter fluctuations were observed in the first sub-layer. In contrast, fluctuations were progressively smoother and smaller the deeper the sub-layer, as also shown by stratigraphic profiles (Figure 16).

According to $d_{s,m90}^-/d_{s,m10}^-$, in the first steps of the simulation, sediment

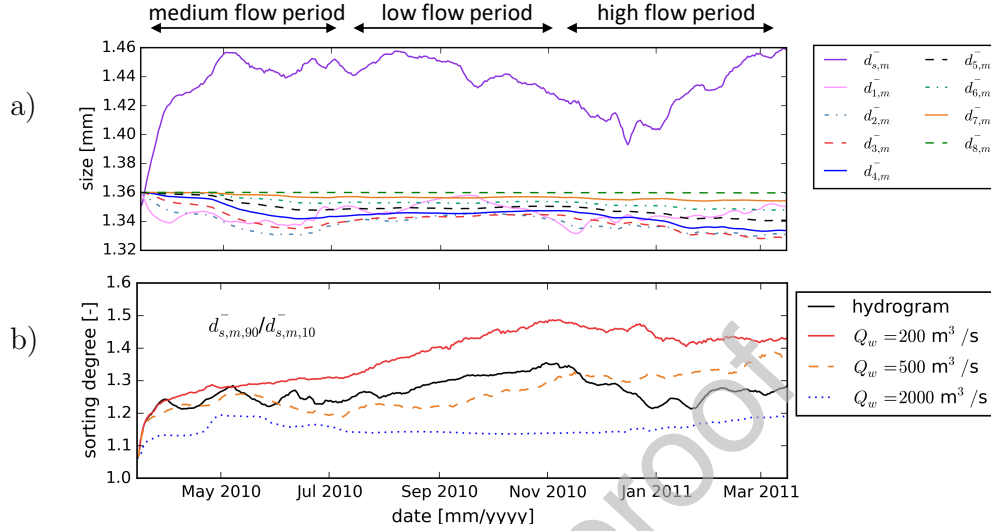


Figure 17: Time-series of a) spatially averaged mean sediment diameter in each sediment layer and b) ratio between the 9th and 1st fractiles used to estimate the degree of spatial sediment sorting with the reference scenario and the three scenarios with constant water discharge.

sorting took time, as illustrated by the low degree of sediment sorting in the sub-layers (Figure 17a, Stages 1 and 2). In this period, the degree of sorting jumped from 1 (i.e., spatially homogeneous) to ≈ 1.2 (i.e., moderately heterogeneous). The period of medium flow (Stages 2 to 6) was associated with stabilization of the degree of sorting toward an equilibrium value of the ratio at ≈ 1.25 . The low flow period, lasting approximately 4 months (Stages 6 to 7), was marked by a progressive increase in degree of sorting, reaching 1.35 in November 2010. Eventually, during the high flow period, the degree of sediment decreased progressively, to values close to 1.20 after the flood of December 11th 2010. In the late stages of the three simulations with constant inflow, the degree of sediment sorting reached equilibrium (Figure 17b), at a value influenced by the flow rate, where higher water discharges invariably increased.

5. Discussion

5.1. Bar pattern and water discharge

The bar mode obtained from the numerical results varied within a range of [1.5-3.5], comparable to the range estimated by on Crosato and Mosselman [19]'s theory. At high flow rates, the bar mode was small (i.e., alternate bars or transverse bar), while higher bar modes were derived for low-flow conditions (i.e., central bars, multiple bars). This variability is consistent with the bar patterns observed in the Loire River [6, 73, 5]. Due to longitudinal changes in width-to-depth ratio, the bar mode increased in the area of channel expansion and decreased in the area of contraction (Figure 6 and 5), as already indicated by Duró et al. [8].

The simulated temporal variation bar mode is generally consistent with the theory, except for September 15th 2010 and December 11th 2010 when the predicted bar modes were overestimated and underestimated, respectively. This can be explained firstly by the theory being formulated for assessment of the long-term response of the river bed assuming constant flow, whereas discharge varied significantly during the flood event of December 11th 2010. The peak discharge of 1,950 m³/s could not trigger formation of alternate bars in the numerical model, because of its short duration. Secondly, the theory can deteriorate for $\beta > 100$, because of the non-linear effects inducing bar merging (and consequent reduction in bar mode) that are not accounted for. As a result, the theory is expected to overestimate bar modes at high width-to-depth ratios, as on September 15th 2010. There was a visible time-lag between bar mode adaptation and flow regime (Figure 4). The bed configuration did not correspond to pure alternate bars ($m = 1$) or central bars characterized by the presence of a bar on each riverside ($m = 2$), which justifies the use of $m = 1 - 2$. In the expansion area, bar mode variations were essentially governed by water discharge variations, as constant flows (runs C, D and E) result in bar modes that did not vary significantly over time.

Numerical results show that the bed topography, i.e., more specifically the bar pattern, influences sediment transport direction and bar migration (Figure 13). In general, the computed bedload magnitude is higher (3 to 5 times) over bars (on the condition that they are submerged) and in the main channel than in pools and lee sides (Figure 11), which is also depicted by local high bedload gradients. Consequently bars advance by the propagation

of steep fronts. The transverse bed slope is found to affect lateral migration of free bars.

Low water discharge enhanced the deviation of bedload direction toward the downslope and increased bar mode and decreased bar wavelength (Figure 13a vs. 13e). Higher modes presented shorter bars, in agreement with the theory [12, 15, 13]. This outcome is also consistent with Singh et al. [18]’s numerical findings on braided channels, where increasing braiding index was related to decreasing bar wavelength and decreased amplitude. This was also shown in the present study (see Table 1 and Figure 16). In any case, even under relatively low flow-rate, bars continued migrating in the study area. This last outcome suggests that bed reworking occurs continuously in sandy gravel bed rivers such as the Loire River. Therefore, numerical modeling of sandy-gravel rivers should be conducted carefully, as, unlike for gravel bed rivers, even low water discharge could contribute to bar dynamics.

5.2. Sediment sorting processes

Numerical results showed that bars presented vertical sediment sorting leading to stratigraphy, in agreement with Bridge [25]’s observations in sandy-gravel bed rivers and with Rodrigues et al. [73, 5]. The numerical approach allows detailed investigation of the processes of sediment sorting, coupling them to bar morphodynamics. In the area of expansion/contraction bars displayed two distinct surface sediment sorting patterns: i) fine in pools and coarse over bar tops in alternate or transverse bar configurations (i.e., low bar modes) and ii) coarse in pools and fine over bar tops in transverse/central bar and multiple bar configurations (i.e., higher bar modes). In every case, the main channel surface was composed of relatively coarse sediment. The sorting pattern computed over the low bar modes ($m < 2$) was consistent with that obtained experimentally [16, 20] and numerically [17, 10] over free alternate bars. As a rule, the presence of coarse sediment over bar tops and in the main channel is due to the high bed shear stress, and fine sediment in pools is due to low shear stresses at pool locations. The sorting pattern computed for high bar modes ($m > 2$) was consistent with that obtained numerically by Singh et al. [18] for partial sediment mobility conditions. For full sediment mobility, Singh et al. [18] showed that no consistent pattern could be detected, apart from coarse sediment in the main channel. In the present study, the major contribution of sand to total bedload transport ($\approx 80\%$) indicates that the system was close to full mobility, even at low-flow (Figure 12). This difference could be due to the choice of the bedload

formula. Singh et al. [18] used Meyer-Peter and Müller [42]’s formula which fails at very high Shields numbers. At low-flow, flow velocity, bed shear stress and consequently sediment transport are close to zero over bar tops. The non-uniformity of spatial flow increased with flow concentration in a narrower channel (Figures 5b and 11c). This spatial re-balancing of sediment transport can be presumed to underlie the distinct sediment sorting patterns observed in braiding systems that appear at relatively low-flow (Figure 16c).

The degree of surface sediment sorting was affected by variations in discharge. High water discharge induced by annual and 2-year floods was followed by a decrease in degree of sorting, while a long period of low-flow was followed by a progressive increase (Figure 17b). This difference seems to be induced by higher sediment mobility. As a result, low bar modes forming at high discharges showed more homogeneous surface sediment than high bar modes (Figures 15 and 17b), as supported by results for constant flow (runs C, D and E). For constant water discharge, the degree of sediment sorting invariably diminished with increasing flow rate.

In the present study, sediment sorting did not significantly impact bar morphodynamics. This may be due to the relatively small difference between the two representative grain diameters, with a ratio of 3.6 which in turn may be due to small grain size (of the order of a few millimeters) and thus low roughness with respect to water depth (of the order of several meters). This outcome is in agreement with Cordier et al. [10], who showed that, at full sediment mobility, sediment sorting had only small effects on free bar morphodynamics and no effect on their time-averaged characteristics. The present results suggest that, in sandy-gravel bed rivers dominated by sand, such as the present case, sediment is fully mobile and, although sorting is observed, it can vanish, just as bars can. Consequently, armoring does not form in the main channel. Sediment sorting can be therefore considered as a ”passive component” of the morphodynamic system as it neither retroactively alters hydraulics nor affects bar properties.

5.3. Limitations and perspectives

The limitations arising from the modeling hypotheses and uncertainty on the data used for this study need to be addressed here, i) to assess the relevance of the numerical approach to processes happening in the field and ii) to consider perspectives to continually improve the modeling and understanding of fluvial bar processes.

873 The first type of limitation lies in the uncertainty of the initial conditions
 874 used in the models in which the initial sediment consisted of a mixture that
 875 was homogeneous over space. Because sediment sorting governs sediment
 876 processes, this can have consequences for model calibration. Moreover, at
 877 least during the first month of computation, numerical results should be in-
 878 terpreted cautiously. The same issue was recently observed numerically with
 879 the formation of free alternate bars with non-uniform sediment in a straight
 880 channel, where the system required a certain lapse of time before reach-
 881 ing morphodynamic equilibrium [10]. Furthermore, the initial granulometry
 882 used in the present study corresponded to the averaged grain size distribution
 883 measured in the middle Loire River, which depends on the time and location
 884 of the granulometric measurements. The lack of field observations during the
 885 low flow period from July to October 2010 increased the uncertainty on bar
 886 patterns in this period of time. The agreement with theoretical predictions
 887 during the low-flow period and the agreement between bar patterns obtained
 888 *in situ* and numerically at the end of 2010 increases the confidence that can
 889 be placed on the morphodynamic model. Uncertainty concerns bed topog-
 890 raphy immediately upstream and downstream of the area of interest, which
 891 may have undergone changes between the date of acquisition (2009) and the
 892 date of interest (2010). This could impact the modeling of bars in the chan-
 893 nel contraction/expansion area, as bars entering the system from upstream
 894 depend on upstream conditions. Lastly, the persistent vestiges of rip-raps in
 895 the main channel highlighted by Claude et al. [6] act as geometrical forcing
 896 structures provided that the overlying sediment layer is fully eroded. The
 897 exact location and elevation of these rigid areas is difficult to determine, and
 898 was estimated from available topographic surveys.

899 Another type of limitation lay in the assumptions chosen for modeling.
 900 As bedload has often been considered to underlie bedform development, sus-
 901 pended load was not taken into account, although sediment suspension could
 902 smooth dunes and bars [71, 72]. In the numerical model, sediment was dis-
 903 cretized into two size fractions; to comply with the bedload model of Wilcock
 904 and Crowe [53], the first fraction was sand present in the mixture and, the
 905 second one corresponded to gravel. Not could only the number of sediment
 906 fractions be increased, but also other methods for decomposing the sedi-
 907 ment mixture into size fractions could be used. Vertical sorting of sediment
 908 is based on the active layer model of Hirano [50], while recent studies on
 909 the ill-posedness of this mathematical model [74, 75, 76] demonstrated that
 910 the solution can be ill-posed under certain conditions. Following Chavarrias

et al. [76], the probability of the present active layer model being ill-posed was reduced by using two sediment size fractions, constant sediment layer thicknesses and Hirano [50]’s formulation for the vertical transfer of sediment. Fluctuations in bed topography and in sediment sorting that are not physics-based were not observed and the numerical model seemed to be rather robust. The study domain was extended 4 km upstream of the study area (i.e., ≈ 14 times channel width), to guarantee sufficient distance for free bars to enter the study area without being unduly influenced by boundary conditions. Finally, the condition of uniformly distributed values of k_s and $\alpha_{k,s}$ over space could be relaxed in the future. Dunes were not represented in the model, and modeling of spatially variable dune-form drag could be improved by using of an appropriate formulation found in the literature for instance [43], but this is outside the scope of the present study. Because superimposition of dunes over bars was observed to enhance the spatial non-uniformity of flow in the upstream channel expansion by Claude et al. [6], non-linear interactions between bar and dune is a topic which deserves more attention.

6. Conclusions

The present study aimed at better understanding the main processes controlling bar morphodynamics mechanisms in contraction/expansion reaches typical of sandy-gravel bed rivers subject to unsteady flow. To this end, we combined a numerical approach and field observations to study bar patterns and sediment sorting in a channel expansion/contraction area with variable flow and heterogeneous sediment composed of a mixture of sand and gravel.

Width-to-depth ratio changes induced by varying water discharge promote competition between low and high bar modes: i.e., from alternate to multiple bar patterns. Linear bar theory supports the numerical results, since the bar modes predicted by the theory fall in the same ranges as those obtained numerically. For this geometrical configuration, we showed that transverse bar migration can come to predominate over longitudinal bar migration. Moreover, bars are found to migrate due to a process of bar top and bar edge erosion, in which bed slope effects contribute actively to lateral bar migration.

While low bar modes are associated with coarse sediment over bar tops and fine sediment in pools, the sorting pattern is inverted for higher bar modes with fine sediment over bar tops and coarser sediment in pools. The

947 surface sediment is coarser and the degree of sediment sorting is higher after
948 periods of low than high flow. This finding is supported by the results of the
949 derived scenarios considering constant water flows. Due to high sediment
950 mobility, general bed surface coarsening does not induce armoring. As a
951 result, bars were found to migrate at all considered discharge rates, while
952 sediment sorting did not significantly modify bar morphodynamics in the
953 study area.

954 **Acknowledgments**

955 The authors gratefully acknowledge the support of Electricité de France
956 (EDF), the reviewers for their high quality and constructive reviews of our
957 manuscript, and the Editor for his careful reading.

958 **Notations**

- B Channel width [m]
 b Degree of non-linearity in the dependence of sediment transport on flow velocity [-]
 C Chézy coefficient [$\text{m}^{1/2}/\text{s}$]
 C_f Equivalent Chézy coefficient due to form drag and skin friction [-]
 C'_f Equivalent Chézy coefficient due to skin friction only [-]
 $c_{b,l}$ Downstream-wise migrating bar celerity [m/d]
 $c_{b,t}$ Transverse migrating bar celerity [m/d]
 d_i Representative diameter of the i^{th} size fraction [m]
 $d_{s,m}$ Median sediment diameter of surface [m]
 $d_{k,m}$ Median sediment diameter of in layer k [m]
 $\bar{d}_{s,m}$ Spatially averaged median sediment diameter of surface [m]
 $\bar{d}_{k,m}$ Spatially averaged median sediment diameter of in layer k [m]
 \bar{d}_X Spatially averaged X^{th} centile of the GSD [m]
 d_{50+X}/d_{50-X} Ratio between opposite centiles or sediment sorting degree [-]
 E Coefficient of calibration for the correction of bedload direction [-]
 $\mathcal{F}_{a:1,i}$ Fraction volume content of i^{th} size fraction in the interface [-]
 $F_{k,i}$ Fraction volume content of i^{th} size fraction in layer k [-]
 F_s Fraction volume content of sand at the bed surface [-]
 g Acceleration due to gravity ($=9.81$) [m/s^2]
 h Water depth [m]
 H_b Bar amplitude [m]
 i_0 Longitudinal bed slope at $t = 0$ s [-]
 k_s Bed roughness height [m]
 L_a Active layer thickness [m]
 m_{th} Theoretical bar mode [-]
 m_{num} Numerical bar mode [-]
 P_0 Bed porosity [-]
 q_b Magnitude of bedload transport rate [m^2/s]
 $\vec{q}_b = (q_{b,X}, q_{b,Y})$ Vector of bedload transport rate [m^2/s]
 q_{b0} Magnitude of bedload transport rate without gravitational effects [m^2/s]
 \vec{q}_{b0} Vector of bedload transport rate without gravitational effects [m^2/s]
 $q_{b,i}$ Magnitude of fractional transport rate of i^{th} size fraction [m^2/s]
 $\vec{q}_{b,i} = (q_{b,i,X}, q_{b,i,Y})$ Vector of fractional transport rate of i^{th} size fraction [m^2/s]
 $q_{b,i,n}$ Magnitude of normal fractional transport rate of i^{th} size fraction [m^2/s]
 $q_{b,i,s}$ Magnitude of stream-wise fractional transport rate of i^{th} size fraction [m^2/s]

- s Coordinate in the current direction [-]
 $\vec{u} = (u, v)$ Flow velocity vector [m/s]
 \bar{u} Spatially averaged flow velocity [m/s]
 u, v Depth-averaged velocity components along x - and y -axis [m/s]
 s Coordinate in the current direction [-]
 $\vec{S}_f = (S_{f,X}, S_{f,Y})$ Friction law vector [-]
 t Physical time [s]
 T_i Coefficient of deviation for the i^{th} size fraction [-]
 u_* Shear velocity [m/s]
 $X-, Y-, Z-$ Axis notation of the Coordinate Cartesian system [-]
 z_b Bed elevation [m]
 z_f Free surface [m]
 α_b Coefficient used to calibrate the sediment transport capacity [-]
 α_i Angle between the vector of fractional transport and x -axis [-]
 $\alpha_{k,s}$ Calibration parameter [-]
 β Width-to-depth ratio [-]
 β_1 Koch and Flosktra's empirical factor for bed slope effects magnitude [-]
 β_2 Talmon's *et al.* empirical factor for bed slope effects deviation [-]
 δ Angle between bottom shear stress and the flow direction [-]
 Δ_s Relative submerged sediment density [-]
 Δt Computational time-step [s]
 Δz_b Evolution of the bed topography with respect to the initial bed elevation [m]
 ϵ_0 Percentage of volumetric matter without voids [-]
 $\eta_{a:1}$ Absolute elevation of the interface [m]
 κ Constant of von Kármán (=0.40) [-]
 λ_b Bar wavelength [m]
 μ Skin friction coefficient [-]
 ∇ Gradient vector field [1/m]
 ν_t Turbulent eddy viscosity term [m²/s]
 $\partial_{x_2} x_1$ Partial derivative of the quantity x_1 in x_2 [x_2/x_1]
 ρ Water density [kg/m³]
 τ Total shear stress [Pa]
 τ_b Bed shear stress [Pa]
 $\tau_{b,i}^*$ Shear stress adimensionnalized by the i^{th} fraction [-]
 χ Decile of the grain size distribution [-]

References

- [1] J. Bridge, R. Demicco, *Earth surface processes, landforms and sediment deposits*, Cambridge University Press, 2008.
- [2] F.-C. Wu, T.-H. Yeh, Forced bars induced by variations of channel width: Implications for incipient bifurcation, *Journal of Geophysical Research: Earth Surface* 110 (2005) 1–22.
- [3] A. P. Nicholas, Modelling the continuum of river channel patterns, *Earth Surface Processes and Landforms* 38 (2013) 1187–1196.
- [4] J. L. Best, P. J. Ashworth, C. S. Bristow, J. Roden, Three-dimensional sedimentary architecture of a large, mid-channel sand braid bar, Jamuna River, Bangladesh, *Journal of Sedimentary Research* 73 (2003) 516–530.
- [5] S. Rodrigues, E. Mosselman, N. Claude, C. L. Wintenberger, P. Juge, Alternate bars in a sandy gravel bed river: generation, migration and interactions with superimposed dunes, *Earth Surface Processes and Landforms* 40 (2015) 610–628.
- [6] N. Claude, S. Rodrigues, V. Bustillo, J.-G. Bréhéret, P. Tassi, P. Jugé, Interactions between flow structure and morphodynamic of bars in a channel expansion/contraction, Loire River, France, *Water Resources Research* 50 (2014) 2850–2873.
- [7] C. L. Wintenberger, S. Rodrigues, J.-G. Bréhéret, M. Villar, Fluvial islands: First stage of development from nonmigrating (forced) bars and woody-vegetation interactions, *Geomorphology* 246 (2015) 305–320.
- [8] G. Duró, A. Crosato, P. Tassi, Numerical study on river bar response to spatial variations of channel width, *Advances in Water Resources* 93 (2016) 21–38. URL: <http://www.sciencedirect.com/science/article/pii/S0309170815002407>. doi:10.1016/j.advwatres.2015.10.003.
- [9] A. Crosato, E. Mosselman, F. Beidmariam Desta, W. S. J. Uijttewaai, Experimental and numerical evidence for intrinsic nonmigrating bars in alluvial channels, *Water Resources Research* 47 (2011) 1–14. URL: <http://dx.doi.org/10.1029/2010WR009714>. doi:10.1029/2010WR009714, w03511.

- 993 [10] F. Cordier, P. Tassi, N. Claude, A. Crosato, S. Rodrigues, D. Pham
 994 Van Bang, Numerical Study of Alternate Bars in Alluvial Chan-
 995 nels With Nonuniform Sediment, *Water Resources Research* 55
 996 (2019) 1–30. URL: [https://agupubs.onlinelibrary.wiley.com/](https://agupubs.onlinelibrary.wiley.com/doi/abs/10.1029/2017WR022420)
 997 [doi/abs/10.1029/2017WR022420](https://agupubs.onlinelibrary.wiley.com/doi/abs/10.1029/2017WR022420). doi:10.1029/2017WR022420.
 998 arXiv:<https://agupubs.onlinelibrary.wiley.com/doi/pdf/10.1029/2017WR022420>.
- 999 [11] E. Hansen, On the formation of meanders as a stability problem.
 1000 Progress Report 13, p.9, Technical Report, Coastal engineering Lab.,
 1001 Technical University Denmark, Basis Research, 1967.
- 1002 [12] F. Engelund, Instability of erodible beds, *Journal of Fluid Mechanics*
 1003 42 (1970) 225–244.
- 1004 [13] G. Seminara, Stability and morphodynamics, *Meccanica* 33 (1998) 59–
 1005 99.
- 1006 [14] P. Hall, Alternating bar instabilities in unsteady channel flows over
 1007 erodible beds, *Journal of Fluid mechanics* 499 (2004) 49–73.
- 1008 [15] N. Struiksmā, K. Olesen, C. Flokstra, H. De Vriend, Bed deformation
 1009 in curved alluvial channels, *Journal of Hydraulic Research* 23 (1985)
 1010 57–79.
- 1011 [16] S. Lanzoni, Experiments on bar formation in a straight flume: 2. Graded
 1012 sediment, *Water Resources Research* 36 (2000) 3351–3363.
- 1013 [17] P. A. Nelson, R. R. McDonald, J. M. Nelson, W. E. Dietrich, Coevo-
 1014 lution of bed surface patchiness and channel morphology: 2. Numerical
 1015 experiments, *Journal of Geophysical Research: Earth Surface* 120 (2015)
 1016 1708–1723.
- 1017 [18] U. Singh, A. Crosato, S. Giri, M. Hicks, Sediment heterogeneity and
 1018 mobility in the morphodynamic modelling of gravel-bed braided rivers,
 1019 *Advances in Water Resources* 104 (2017) 127–144.
- 1020 [19] A. Crosato, E. Mosselman, Simple physics-based predictor for the num-
 1021 ber of river bars and the transition between meandering and braiding,
 1022 *Water Resources Research* 45 (2009) 1–12.

- [20] P. A. Nelson, R. R. McDonald, J. M. Nelson, W. E. Dietrich, Coevolution of bed surface patchiness and channel morphology: 1. Mechanisms of forced patch formation, *Journal of Geophysical Research: Earth Surface* 120 (2015) 1687–1707.
- [21] J. Sun, B. Lin, H. Yang, Development and application of a braided river model with non-uniform sediment transport, *Advances in water resources* 81 (2015) 62–74.
- [22] A. R. Bankert, P. A. Nelson, Alternate bar dynamics in response to increases and decreases of sediment supply, *Sedimentology* 65 (2018) 702–720. URL: <https://onlinelibrary.wiley.com/doi/abs/10.1111/sed.12399>. doi:10.1111/sed.12399. arXiv:<https://onlinelibrary.wiley.com/doi/pdf/10.1111/sed.12399>.
- [23] H. Miwa, A. Daido, J. Yokogawa, Growth and transformation of alternate bars under sinusoidal wave flood conditions, *Bulletin of Maizuru National College of Technology* 38 (2003) 81–88. URL: <http://ci.nii.ac.jp/naid/110000992944/en/>.
- [24] P. A. Nelson, J. A. Morgan, Flume experiments on flow and sediment supply controls on gravel bedform dynamics, *Geomorphology* n/a (2018) n/a–n/a.
- [25] J. S. Bridge, *Rivers and floodplains: forms, processes, and sedimentary record*, John Wiley & Sons, 2003.
- [26] S. Zen, G. Zolezzi, M. Tubino, A theoretical analysis of river bars stability under changing channel width, *Advances in Geosciences* 39 (2014) 27–35.
- [27] A. Crosato, *Analysis and modelling of river meandering*, TU Delft, Delft University of Technology, 2008.
- [28] R. Luchi, J. Hooke, G. Zolezzi, W. Bertoldi, Width variations and mid-channel bar inception in meanders: River Bollin (UK), *Geomorphology* 119 (2010) 1–8.
- [29] A. Nelson, K. Dubé, Channel response to an extreme flood and sediment pulse in a mixed bedrock and gravel-bed river, *Earth Surface Processes and Landforms* 41 (2015) 178–195.

- [30] J. M. Nelson, The initial instability and finite-amplitude stability of alternate bars in straight channels, *Earth-Science Reviews* 29 (1990) 97–115. URL: <http://www.sciencedirect.com/science/article/pii/001282529090030Y>. doi:10.1016/0012-8252(0)90030-Y.
- [31] R. Repetto, M. Tubino, C. Paola, Planimetric instability of channels with variable width, *Journal of Fluid Mechanics* 457 (2002) 79–109.
- [32] M. García, Y. Niño, Dynamics of sediment bars in straight and meandering channels: experiments on the resonance phenomenon, *Journal of Hydraulic Research* 31 (1993) 739–761.
- [33] P. J. Whiting, W. E. Dietrich, Experimental constraints on bar migration through bends: Implications for meander wavelength selection, *Water Resources Research* 29 (1993) 1091–1102. URL: <http://dx.doi.org/10.1029/92WR02356>. doi:10.1029/92WR02356.
- [34] F.-C. Wu, Y.-C. Shao, Y.-C. Chen, Quantifying the forcing effect of channel width variations on free bars: Morphodynamic modeling based on characteristic dissipative Galerkin scheme, *Journal of Geophysical Research: Earth Surface* 116 (2011) 5717–5734. URL: <https://agupubs.onlinelibrary.wiley.com/doi/abs/10.1029/2010JF001941>. doi:10.1029/2010JF001941. arXiv:<https://agupubs.onlinelibrary.wiley.com/doi/pdf/10.1029/2010JF001941>.
- [35] L. D. Bittner, Y. Nino, M. H. Garcia, River Bed Response to Channel Width Variation: Theory and Experiments, Technical Report, University of Illinois, Urbana-Champaign, 1995.
- [36] N. Claude, Processus et flux hydro-sédimentaires en rivière sablo-graveleuse: influence de la largeur de section et des bifurcations en Loire moyenne (France), Ph.D. thesis, Tours, 2012.
- [37] K. Tockner, U. Uehlinger, C. T. Robinson, *Rivers of Europe*, volume 1, Elsevier, 2008.
- [38] S. Rodrigues, P. Le Hir, F. Moatar, N. Claude, Transferts de particules dans le continuum fluvio-estuarien, *La Loire fluviale et estuarienne : un milieu en evolution* 1 (2016) 85–111.

- [39] S. Rodrigues, J.-G. Br        , J.-J. Macaire, F. Moatar, D. Nistoran, P. Jug  , Flow and sediment dynamics in the vegetated secondary channels of an anabranching river: the Loire River (France), *Sedimentary Geology* 186 (2006) 89–109.
- [40] K. M. Andreadis, G. J.-P. Schumann, T. Pavelsky, A simple global river bankfull width and depth database, *Water Resources Research* 49 (2013) 7164–7168.
- [41] N. Claude, S. Rodrigues, V. Bustillo, J.-G. Br        , J.-J. Macaire, P. Jug  , Estimating bedload transport in a large sand-gravel bed river from direct sampling, dune tracking and empirical formulas, *Geomorphology* 179 (2012) 40–57.
- [42] E. Meyer-Peter, R. M      , Formulas for bed-load transport, in: *International Association for Hydraulic Structures Research*, IAHR, 1948.
- [43] L. C. Van Rijn, Sediment transport, part III: bed forms and alluvial roughness, *Journal of hydraulic engineering* 110 (1984) 1733–1754.
- [44] A. B. de Saint-Venant, Th       du mouvement non permanent des eaux, avec application aux crues des rivi       et    l'introduction des mar     dans leurs lits, *Comptes Rendus des s         de l'Acad       des Sciences* 73 (1871) 237–240.
- [45] T. Weiyan, *Shallow Water Hydrodynamics: Mathematical Theory and Numerical Solution for a Two-dimensional System of Shallow Water Equations*, number vol. 55 in *Elsevier oceanography series*, Water & Power Press, 1992.
- [46] I. Nezu, H. Nakagawa, G. H. Jirka, Turbulence in open-channel flows, *Journal of Hydraulic Engineering* 120 (1994) 1235–1237.
- [47] C. B. Vreugdenhil, *Numerical methods for shallow-water flow*, volume 13, Springer Science & Business Media, 2013.
- [48] J. Nikuradse, *Laws of flow in rough pipes*, NACA, 1950.
- [49] F. M. Exner, *Zur physik der d      *, H      , 1920.
- [50] M. Hirano, *River bed degradation with armoring*, Ph.D. thesis, Japanese Society of Civil Engineering, 1971.

- 1117 [51] M. Church, J. K. Haschenburger, What is the active layer?, *Water*
 1118 *Resources Research* 53 (2017) 5–10. URL: [http://dx.doi.org/10.1002/](http://dx.doi.org/10.1002/2016WR019675)
 1119 [2016WR019675](http://dx.doi.org/10.1002/2016WR019675). doi:10.1002/2016WR019675.
- 1120 [52] P. Ashmore, S. Peirce, P. Leduc, Expanding the Active
 1121 Layer: Discussion of Church and Haschenburger (2017) What
 1122 is the Active Layer? *Water Resources Research* 53, 510,
 1123 Doi:10.1002/2016WR019675, *Water Resources Research* 54 (2018)
 1124 1425–1427. URL: [https://agupubs.onlinelibrary.wiley.com/](https://agupubs.onlinelibrary.wiley.com/doi/abs/10.1002/2017WR022438)
 1125 [doi/abs/10.1002/2017WR022438](https://agupubs.onlinelibrary.wiley.com/doi/abs/10.1002/2017WR022438). doi:10.1002/2017WR022438.
 1126 arXiv:<https://agupubs.onlinelibrary.wiley.com/doi/pdf/10.1002/2017WR022438>.
- 1127 [53] P. R. Wilcock, J. C. Crowe, Surface-based transport model for mixed-
 1128 size sediment, *Journal of Hydraulic Engineering* 129 (2003) 120–128.
- 1129 [54] A. Recking, G. Piton, D. Vazquez-Tarrio, G. Parker, Quantifying the
 1130 Morphological Print of Bedload Transport, *Earth Surface Processes and*
 1131 *Landforms* 41(6) (2015) 809–822.
- 1132 [55] F. Koch, C. Flokstra, Bed Level Computations for Curved Alluvial
 1133 Channels: Prepared for the 19th IAHR Congress, New Delhi, India,
 1134 February 1981, Waterloopkundig Laboratorium, 1980.
- 1135 [56] C. Van der Meer, E. Mosselman, C. Sloff, B. Jagers, G. Zolezzi,
 1136 M. Tubino, Numerical simulations of upstream and downstream
 1137 overdeepening, in: RCEM 2011: Proceedings of the 7th IAHR Sym-
 1138 posium of River, Coastal and Estuarine Morphodynamics, Beijing, China,
 1139 6-8 September 2011, Citeseer, 2011.
- 1140 [57] G. Zolezzi, G. Seminara, Downstream and upstream influence in river
 1141 meandering. Part 1. General theory and application to overdeepening,
 1142 *Journal of Fluid Mechanics* 438 (2001) 183–211.
- 1143 [58] O. Cabrit, Modélisation des flux pariétaux sur les tuyères des moteurs
 1144 à propergol solide, Ph.D. thesis, Montpellier 2, 2009.
- 1145 [59] L. V. Bendegom, Some considerations on river morphology and river
 1146 improvement, *De Ingenieur* vol. 59–4, pp. B1–11, Dutch. English trans-
 1147 lation: Nat. Res. Council of Canada, Technical Translation 1054 (1947)
 1148 1963.

- [60] A. Talmon, N. Struiksmā, M. Van Mierlo, Laboratory measurements of the direction of sediment transport on transverse alluvial-bed slopes, *Journal of Hydraulic Research* 33 (1995) 495–517.
- [61] A. Mendoza, J. D. Abad, E. J. Langendoen, D. Wang, P. Tassi, K. E. K. Abderrezzak, Effect of Sediment Transport Boundary Conditions on the Numerical Modeling of Bed Morphodynamics, *Journal of Hydraulic Engineering* 143 (2016) .
- [62] M. H. García, Sedimentation engineering, Processes, Measurements, Modeling, and Practice. ASCE Manuals and Reports on Engineering Practice 110 (2008) 1–1132.
- [63] F. Huthoff, Theory for flow resistance caused by submerged roughness elements, *Journal of Hydraulic Research* 50 (2012) 10–17. URL: <https://doi.org/10.1080/00221686.2011.636635>. doi:10.1080/00221686.2011.636635. arXiv:<https://doi.org/10.1080/00221686.2011.636635>.
- [64] J. Hervouet, E. Razafindrakoto, C. Villaret, Dealing with dry zones in free surface flows: a new class of advection schemes, in: A. Barton (Ed.), *Proceedings of the 34th World Congress of the International Association for Hydro-Environment Research and Engineering: 33rd Hydrology and Water Resources Symposium and 10th Conference on Hydraulics in Water Engineering*, Australia, 2011, pp. 4103–411.
- [65] F. Cordier, Bars morphodynamics in trained rivers with heterogeneous sediment, Ph.D. thesis, 2018.
- [66] C. A. Vionnet, P. A. Tassi, J. P. Martin Vide, Estimates of flow resistance and eddy viscosity coefficients for 2D modelling on vegetated floodplains, *Hydrological Processes* 18 (2004) 2907–2926. URL: <https://onlinelibrary.wiley.com/doi/abs/10.1002/hyp.5596>. doi:10.1002/hyp.5596. arXiv:<https://onlinelibrary.wiley.com/doi/pdf/10.1002/hyp.5596>.
- [67] J. Sutherland, A. Peet, R. Soulsby, Evaluating the performance of morphological models, *Coastal engineering* 51 (2004) 917–939.

- [68] J. Bosboom, A. J. H. M. Reniers, A. P. Luijendijk, On the perception of morphodynamic model skill, *Coastal Engineering* 94 (2014) 112–125. URL: <http://www.sciencedirect.com/science/article/pii/S0378383914001604>. doi:10.1016/j.coastaleng.2014.08.008.
- [69] F. Baart, M. van Ormondt, J. van Thiel de Vries, M. van Koningsveld, Morphological Impact of a Storm Can Be Predicted Three Days Ahead, *Computational Geosciences* 90 (2016) 17–23. URL: <http://dx.doi.org/10.1016/j.cageo.2015.11.011>. doi:10.1016/j.cageo.2015.11.011.
- [70] G. Dam, M. Wegen, R. J. Labeur, D. Roelvink, Modeling centuries of estuarine morphodynamics in the Western Scheldt estuary, *Geophysical Research Letters* 43 (2016) 3839–3847. URL: <https://agupubs.onlinelibrary.wiley.com/doi/abs/10.1002/2015GL066725>. doi:10.1002/2015GL066725. arXiv:<https://agupubs.onlinelibrary.wiley.com/doi/pdf/10.1002/2015GL066725>.
- [71] S. T. Meles, Effects of suspended sediments on river bars, Master's thesis, Unesco IHE Delft, 2015.
- [72] S. Naqshband, J. Ribberink, S. Hulscher, D. Hurther, Sediment transport distribution along developing sand dunes, in: A. Schleiss, G. De Cesare, M. Franca, M. Pfister (Eds.), *River Flow 2014*, Taylor & Francis, United Kingdom, 2014, pp. 1039–1044.
- [73] S. Rodrigues, N. Claude, P. Juge, J.-G. Breheret, An opportunity to connect the morphodynamics of alternate bars with their sedimentary products, *Earth Surface Processes and Landforms* 37 (2012) 240–248. URL: <http://dx.doi.org/10.1002/esp.2255>. doi:10.1002/esp.2255.
- [74] G. Stecca, A. Siviglia, A. Blom, Mathematical analysis of the Saint-Venant-Hirano model for mixed-sediment morphodynamics, *Water Resources Research* 50 (2014) 7563–7589.
- [75] G. Stecca, A. Siviglia, A. Blom, An accurate numerical solution to the Saint-Venant-Hirano model for mixed-sediment morphodynamics in rivers, *Advances in Water Resources* 93 (2016) 39–61.
- [76] V. Chavarrias, G. Stecca, A. Blom, Ill-posedness in modeling mixed sediment river morphodynamics, *Advances in Water Resources* 114 (2018)

1212 219–235. URL: [http://www.sciencedirect.com/science/article/](http://www.sciencedirect.com/science/article/pii/S0309170817302658)
1213 [pii/S0309170817302658](http://www.sciencedirect.com/science/article/pii/S0309170817302658). doi:10.1016/j.advwatres.2018.02.011.

Journal Pre-proof

Declaration of interests

☒ The authors declare that they have no known competing financial interests or personal relationships that could have appeared to influence the work reported in this paper.

☐ The authors declare the following financial interests/personal relationships which may be considered as potential competing interests: